The Positional Effect of an Immobilized Re Tricarbonyl Catalyst for CO_2 Reduction

*Jeremiah C. Choate, Israel Silva Jr., Po Ching Hsu, Kaylyn Tran, and Smaranda C. Marinescu**

Department of Chemistry, University of Southern California, Los Angeles, California 90089, United States

KEYWORDS: aryldiazonium salts, electrografting, electropolymerization, Re bipyridine, electrocatalysis, CO_2 conversion

*email: smarines@usc.edu

Abstract:

The storage of renewable energy through the conversion of CO_2 to CO provides a viable solution for the intermittent nature of these energy sources. The immobilization of rhenium(I) tricarbonyl molecular complexes is presented through the reductive coupling of bisdiazonium aryl substituents. The heterogenized complex was characterized through ultra–visible, attenuated total reflectance, infrared reflection absorption spectroscopy, and X-ray photoelectron spectroscopy to probe the electronic structure of the immobilized complex. In addition, studies of cyclic voltammetry, controlled potential electrolysis, and electronic impedance spectroscopy were conducted to examine the CO_2 reduction activity. The structure and CO_2 reduction performance were compared with a previously reported immobilized rhenium(I) tricarbonyl molecular complex to probe the effect of varying the tethering of the aryl substituent from the 5,5′- position to the 4,4′- position of the 2,2′- bipyridine backbone. The immobilized complex on carbon cloth at the 4,4′- position provided excellent selectivity (FE_{CO} > 99%) and maximum TON_{CO} and TOF_{CO} values of 3359 and 0.9 s^{-1}, respectively, without the addition of a Brønsted acid source. A non-aqueous flow cell demonstrated the stability of this complex during a 5 h electrolysis. Tethering at the 4,4′- position, compared to the 5,5′- position, yielded lower overall activity for CO_2 reduction and was attributed to the difference in growth morphology and formation of aggregations, due to Re-Re dimer formation and π- π stacking interactions within the metallopolymer matrix. For carbon cloth substrates, an optimized catalyst loading was determined to be 44.6 ± 11 nmol/cm^2.

Introduction:

With population expansion, the rise in energy demand, and the negative environmental impacts of climate change, the requirement for developing sustainable energy technology is paramount.[1] With the potential availability of solar energy (79,000 TWyr) hitting the earth's surface, and wind energy as a close second, there is the capability of meeting the world's energy demand several times over.[2] However, due to the intermittent nature of solar and wind energy, there is an inherent mismatch between the use of renewable energy and demand.[3] To circumvent this, a solution lies in using renewable energy-derived electricity to drive the storage and conversion of chemical fuels. The electrocatalytic conversion of CO_2 to CO can provide a viable means of storing energy in the form of chemical bonds.[4] This conversion can also help reduce the rise in atmospheric carbon dioxide, as CO_2 is the primary greenhouse gas contributing to climate change.

The *fac*-Re(2,2′-bipyridine)$(CO)_3Cl$ (ReBpy) complex was first reported as a CO_2 reduction photocatalyst in 1983 by Hawecker, Lehn, and Ziessel.[5] The following year, Lehn and coworkers published a report where the ReBpy was used as an electrocatalyst and resulted in 98% Faraday Efficiency (FE) for CO_2 to CO conversion.[6] From this foundational work, and the continued research on the homogeneous ReBpy as CO_2 reduction catalyst, this complex is of particular interest in this report. Correspondingly, homogeneous catalysts are attractive due to their tunable ligand environment and their resulting chemical properties leading to catalytic selectivity/activity modulation, well-defined catalytic active sites, and the subsequent establishment of structure-mechanism-activity relationships.[7] However, the drawbacks of employing molecular catalysts consists in their limited solubility, poor recyclability after use, and their poor utilization as only the amount that is present in the diffusion layer participates in catalysis, rendering the rest of the catalyst solution in the bulk as non-active, in addition to mass-transport limitations which result from a greater distance of diffusion from the bulk to the electrode.[7]

The immobilization of homogeneous catalysts represents an attractive solution to the setbacks stated above.[8,9] The heterogenization developed thus far can be organized into several immobilization methods: (i) periodic, (ii) non-covalent, and (iii) covalent.[7] Sun and coworkers reported a periodic immobilization, where ReBpy was incorporated into a metal-organic framework (MOF) and deposited as a thin film onto fluorine-doped tin oxide substrates for electrocatalytic CO_2 reduction.[10] Similarly, our group has previously reported the incorporation of ReBpy into MOFs and a covalent-organic framework (COF) for CO_2 reduction.[11,12] However, MOFs and COFs typically display low electronic conductivity and have low stability under reductive conditions, which limits their applications in electrocatalysis.[13] An alternative approach was reported by Gray and coworkers previously utilizing pyrene moieties to non-covalently immobilize ReBpy into the basal plane of a highly oriented pyrolytic graphite substrate through π-π interactions.[14] Unfortunately, most non-covalent immobilized catalysts experience decay, subsequent leaching of the catalyst in solution during the prolong experiments to test stability, and slow electron transfer, which is due to weak van der Waals interactions between the catalyst and the substrate.[7] The covalent immobilization method can overcome these shortcomings and can be divided into two subclasses, chemical reactions, and electrochemical reactions. Surendranath and coworkers have reported an example of the prior, where ReBpy was linked to a graphitic electrode through pyrazine linkages for electrochemical CO_2 reduction.[15] Yet, covalent immobilization through chemical reactions involves the development of arduous reaction strategies that covalently

link the molecules onto the substrates. Conversely, electrochemical polymerization provides an easier alternative to tethering molecules covalently onto substrates to form catalytic active films.

After the report by Lehn, which outlined the electrocatalytic activity of ReBpy, Meyer and coworkers conducted a study of electrochemically polymerizing Re(v-Bpy) (v-Bpy = 4-vinyl-4′-methyl-2,2′-bipyridine) onto a platinum substrate.[16,17] This report demonstrated that after polymerization, the films were more efficient for CO_2 reduction, as turnover numbers (TONs) were 20 times larger when compared to those for the monomer in solution. However, due to the flexibility, and radicals produced from the vinyl substituent upon electropolymerization, the films showed cycling stability issues, which were a result of the formation of Re-C and Re-Re dimer bonds.[16,17] Due to these complications, other coupling agents are required to form effective tethering to substrates. Previously, Pinson and coworkers introduced the use of aryl diazonium salts to modify carbon electrodes in 1992.[18] The advantages of diazonium salts, over other coupling agents, are their facile preparation, fast electroreduction, a wide range of functional groups, and robust surface covalent bonding.[16] Nervi and coworkers made use of this coupling method to covalently tether MBpy (where M = Mn or Re) complexes to the surface of glassy carbon electrodes.[19] Specifically for ReBpy, the immobilization resulted in films with better performance – a 60-fold increase in the activity was observed when compared to the homogeneous catalyst in acetonitrile. Comparatively, polymer films formed with conjugated bipyridine backbones displayed increased structural stability.[20] Thus, the use of diazonium salt coupling and the formation of conjugated backbones provides a suitable system to form electroactive films.

Our group has previously reported on the application of electropolymerization to form catalytic films of surface-immobilized rhenium(I) bipyridine polymers.[21] The reduction of bis(diazonium) salts led to the covalent surface attachment of the ReBpy to a wide range of electrodes. Electrocatalytic studies displayed faradaic efficiency (FE) and turnover frequency (TOF) of 99% and 0.50 s^{-1}, respectively. Interested in the exploration of analogous catalysts for this system, functionalization of the tethering of the rhenium bis(diazonium) complex from the 5,5′- position to the 4,4′- position of the bipyridine backbone was pursued to elucidate changes in the catalytic activity, electronic structure, and growth morphology of the respective films. Within this report, immobilization of rhenium complexes at the 4,4′- position of the bipyridine backbone resulted in ReBpy-containing films with decreased electron density at the metal center, decreased conjugation, Re-Re dimer formation, and change in growth morphology. This system was investigated through glassy carbon and carbon cloth substrates to probe the immobilized catalyst in terms of electronic structure and CO_2 reduction activity. Specifically, tethering the rhenium complex at the 4,4′- position onto carbon cloth substrates resulted in ReBpy-containing films that displayed excellent selectivity (FE_{CO} > 99%) and maximum TON_{CO} and TOF_{CO} values of 3359 and 0.9 s^{-1}, respectively, although, this system yielded a less catalytically active system, when compared to analogous ReBpy tethered at the 5,5′- position. The variance in CO_2 activity was attributed to the formation of aggregations, due to Re-Re dimer formation and π-π stacking interactions within the metallopolymer matrix. An optimized catalyst loading was determined to be 44.6 ± 11 nmol/cm^2.

EXPERIMENTAL SECTION:

Materials and Synthesis.

All manipulations of air- and moisture-sensitive materials were conducted under nitrogen atmosphere in a Vacuum Atmospheres glovebox or on a dual manifold Schlenk line with oven-

dried glassware. Water was deionized with the Millipore Synergy system (18.2 MΩ·cm). Acetonitrile, diethyl ether, and toluene were degassed with nitrogen, passed through activated alumina columns, and stored over 3Å or 4Å Linde-type molecular sieves in an inert atmosphere. [2,2′-bipyridine]-4,4′-diamine (TCI Chemicals, 98+%), Rhenium pentacarbonyl chloride (Thermo Fisher Scientific, 98%), and nitrosonium tetrafluoroborate (Sigma Aldrich, 98%) were purchased from Fisher Scientific. A rhenium standard solution (Inorganic Ventures, 997 μg/mL Re in 3% (v/v) nitric acid) was purchased from VWR International LLC. All other chemical reagents were purchased from commercial vendors and used without further purification.

[2,2'-bipyridine]-4,4'-diaminechlororhenium(I). The rhenium [2,2′-bipyridine]-4,4′-diamine complex was synthesized using a previously reported metalation procedure for the rhenium 5,5′-diamine analogue. The [2,2′-bipyridine]-4,4′-diamine ligand was refluxed in a toluene solution with rhenium (I) pentacarbonyl chloride (**Scheme S1**),[22] and the reaction mixture was allowed to stir for 18 hours. The resulting bright yellow precipitant was collected by vacuum filtration and purified through hot filtration with ethyl acetate. After washing with ether, the resulting bright yellow solid formed with an 88% yield. ^{1}H-NMR (400 MHz, CD_3CN) δ 8.34 (2H, d), 7.28 (2H, s), 6.67 (2H, d), 5.66 ppm (4H, s).

[2,2'-bipyridine]-4,4'-diazoniumchlororhenium(I). Oven-dried 50 mL and 25 mL Schlenk flasks with adaptors and stir bars were cooled in the antechamber of the glovebox before being brought in. Following assembly, the 50 mL flask was charged with 25.2 mg (0.216 mmol) of $NOBF_4$ and 0.9 mL of acetonitrile. The 25 mL flask was charged with 44.8 mg (0.0911 mmol) of [2,2′-bipyridine]-4,4′-diaminechlororhenium(I) and 1.9 mL of acetonitrile. The 50 mL flask was then placed on the Schlenk line with cycles of N_2 and vacuum. The [2,2′-bipyridine]-4,4′-diaminechlororhenium(I) was subjected to sonication for 10 mins before an additional placement on the Schlenk line. Both flasks were cooled in an acetonitrile/dry ice bath (-40 °C) before the [2,2′-bipyridine]-4,4′-diaminechlororhenium(I) suspension was added dropwise to the $NOBF_4$ solution. An immediate dark purple coloration occurred. This solution was stirred for about 1 hour before the addition of 35 mL of dried anhydrous diethyl ether. The resulting adhesive-violet-colored precipitant was collected by vacuum filtration and dried with a minimal amount of diethyl ether. The precipitant was collected and stored in the dark at -27 °C. ^{1}H-NMR (500 MHz, CD_3CN): δ 9.70, 9.35, and 8.66 ppm. ^{19}F-NMR (500 MHz, CD_3CN): δ -150.8 ppm.

Note: Careful attention should be placed on the stability of 4,4′-(bis)diazonium salts. Diazonium salts are slightly unstable even when stored in a freezer,[23] for this reason, the diazonium salts were immediately used in electrochemical grafting. Additionally, no bisdiazonium salts were used after 5 days of being synthesized.

Preparation of Carbon Cloth Samples. Carbon Cloth Electrodes (CCEs) (99.5% carbon) were purchased from Fuel Cell Earth LLC. The cloth was cut into 1 × 4 cm^2 pieces and treated with 9.7 M HCl solution for 1.5 hours to remove trace metal impurities, followed by soaking in Mili-Q water and rinsing thoroughly with Mili-Q water. Cycles of 10-minute sonication in Mili-Q water, acetone, Mili-Q water were subsequently applied. The CCE was then allowed to dry in air overnight before use.

Preparation of FTO Samples. Flourine-doped Tin Oxide (FTO) were cut into 1 × 4 cm^2 pieces and cleaned with a series of 10-minute sonication cycles in soapy water, acetone, isopropanol, and Mili-Q water and allowed to dry in air overnight before use.

Modification of Electrode Samples. Electrodes of CCE, FTO, Glassy Carbon and gold electrodes were modified based on our previously optimized procedure.[21] Modifications to this procedure were made to facilitate the parallel-modification of up to four electrodes. A stock solution of 0.5 mM bis(diazonium) monomer was prepared in an anhydrous acetonitrile solution with 0.1 M [nBu$_4$][PF_6] supporting electrolyte. The bulk of the grafting stock solution was kept in a dry ice/acetonitrile bath. The volume of the stock solution depends on the number of electrodes being grafted; 10 mL of fresh stock solution was used for each grafted electrode. The Pt wire was polished and heated to red hot prior to use. An oven-dried, nitrogen-purged cyclic voltammetry cell was capped with a Teflon adapter holding the working, pseudo-reference Ag wire, and Pt counter electrodes. A fresh 10 mL aliquot of the grafting stock solution was injected into the cell and a series of cyclic voltammetry (CV) scans were run between -0.2 V and -1.2 V vs. vs. $Fc^{+/0}$ at a scan rate of 1 V/s. Electropolymerizations were referenced externally.

Physical Methods:

NMR Spectroscopy
Proton NMR spectra were acquired at room temperature using Varian (Mercury 400 2-Channel and VNMRS-500 2-Channel) spectrometers and referenced to the residual ^{1}H resonances of the deuterated solvent (^{1}H: CD_3CN-d_3, δ 1.94 ppm).

UV-Vis NIR spectroscopy
Spectra were obtained using a Lambda 950 UV/Vis/NIR Spectrophotometer. Molecular samples were analyzed in transmittance mode with an air-free 1 cm quartz cuvette, and the spectrum measured for a blank acetonitrile sample was subtracted as background. Modified FTO samples were studied in transmittance mode and the spectrum measured for an unmodified FTO substrate was subtracted as background.

X-ray Photoelectron Spectroscopy
XPS data were collected using a Kratos AXIS Ultra instrument. The monochromatic X-ray source was the Al K α line at 1486.6 eV. Low-resolution survey spectra were acquired between binding energies of 1–1200 eV. The Survey scan was collected at a pass energy 160 eV. Higher-resolution detailed scans, with a resolution of ~0.1 eV, were collected on individual XPS lines of interest at pass energy of 20 eV. The sample chamber was maintained at < 2 × 10^{-8} Torr. A charge neutralizer was employed to remove build-up charge on the sample surface during XPS experiments. The XPS data were analyzed using the CasaXPS software.

FT-IR
Fourier-transform infrared spectroscopy (FT-IR) spectra were acquired using a Nicolet™ iS20 FTIR Spectrometer. Reflectance spectra were collected using a VeeMAX III specular reflectance accessory from Pike Instruments. Samples were positioned face-down over an aperture (3/8" diameter). All IRRAS measurements were collected with a 56° angle of incidence under vacuum pressure with 1 cm^{-1} resolution. Polarization studies were performed with a ZnSe polarizing lens

purchased from Pike Instruments. The spectra measured for unmodified substrates under identical experimental parameters (angle, polarization, and resolution) were subtracted as background. Studies were performed at 1 cm^{-1} resolution with 128 or 200 scans. ATR-FTIR measurements for complex **1** were performed in the ATR mode.

SEM

Scanning electron microscopy (SEM) was performed on a NanoSEM 450 scanning electron microscope using an accelerating voltage of 5 or 10 kV.

ICP-OES

Inductive Coupled Plasma Optical Emission Spectroscopy (ICP-OES) measurements were performed using a Thermo Scientific iCAP 7000 ICP-OES and were used to determine the amount of Re deposited on the surface of **2**-CC substrates. The raw intensity data was converted to concentration with the use of a calibration curve generated from a series of standards in aqueous 3% nitric acid solutions containing known concentrations of Re. The calibration standards were prepared by dilution of a 997 ± 4 μg/mL Re standard solution (3% v/v HNO_3). The serial standard concentrations were 100, 10, 1, 0.1, 0.01 ppm of Re. The modified electrodes **2**-CC were digested by sonicating in 2 mL of nitric acid overnight and then diluted to a final volume of 100 mL with Millipore water. After filtering, the concentration of the modified electrodes was measured and converted to Re concentration referenced to the electrochemically active geometrical surface area = 1.5 cm^2. Each modified electrode sample was measured as a set of triplicate data sets and reported as the average.

Post-catalysis analysis of the working electrode solution was done by diluting a 10 μL aliquot of the working electrode solution to 100 mL and filtering before subjecting to ICP-OES analysis.

Electrochemistry:

Cyclic Voltammetry

Electrochemistry experiments were carried out in acetonitrile solution with 0.1 M $TBAPF_6$ electrolyte using a Pine potentiostat for cyclic voltammetry measurements and VersaSTAT 3 potentiostat for the EIS measurements. The experiment was carried out in a three-electrode configuration electrochemical cell under a nitrogen or CO_2 atmosphere using an 3 mm diameter glassy carbon, FTO, or carbon cloth as the working electrode, a pseudo-reference electrode of a silver wire purchased from VWR, and a platinum wire as the auxiliary electrode purchased from Alfa Aesar. The reference electrode was isolated in a glass capillary with a Vycor frit. Ohmic drop was compensated using the positive feedback compensation implemented in the instrument. All experiments, except for electropolymerization (referenced externally), were referenced relative to ferrocene (Fc) with the $Fe^{3+/2+}$ couple at 0.0 V, and all CVs were first scanned anodically and subsequently returned cathodically.

Controlled Potential Electrolysis and Gas Chromatography

CPE measurements were conducted in a two-chambered H cell. In the first chamber, the working and reference electrodes were immersed in 40 mL of 0.1 M tetrabutylammonium hexafluorophosphate ($TBAPF_6$) in acetonitrile for non-aqueous conditions. The counter electrode (unmodified carbon cloth) was placed in the second chamber in 20 mL of 0.1 M $TBAPF_6$ in

acetonitrile. The two chambers were separated by a fine porosity glass frit and the reference electrode was placed in a separate compartment connected by a Vycor tip. Carbon cloth electrodes (Fuel Cell Earth, Inc.) were used as the modified working or unmodified auxiliary electrodes. For gas chromatography experiments, 2 mL of gas were withdrawn from the headspace of the H cell with a gas-tight syringe. This was injected into a gas chromatography instrument Shimadzu GC-2010-Plus equipped with a BID detector and a Restek ShinCarbon ST Micropacked column or a Nexis GC-2030 equipped with a PTCD and FID detector. Faradaic efficiencies were determined by dividing the amount of CO produced as measured by gas chromatography by the amount of CO expected based on the total charge measured during controlled potential electrolysis. For each experiment, the controlled-potential electrolysis measurements were performed at least twice (with two samples prepared under identical conditions), leading to similar behavior.

Non-aqueous CO_2 reduction Flow Cell

Flow cell system's unique design allows for different electrodes to be tested under a controlled environment. Implementing air/oxygen sensitive catalysts into the flow cell system can provide longer stability and a prolonged lifecycle for the system where the electrolytes can survive for lengthily tests. Unlike other battery cell setup, like coin cells which have all its compartments encased inside the coin, the flow cell is a liquid state system.

The flow cell was assembled (**Figure S29**) through custom-made cell hardware (Electrochem Inc.). The cell block consists of layers of conducting blocks, the first outer layer is made of gold-plated charge carrier copper plates, and the Potentiostat (Solartron Metrology) is connected to the charge carrier during the experiments where a potential of -2.6 V was applied. With the reference being the counter electrode in this system, the potential is referenced to the OER potential in basic media. Sandwiched between the charge carriers are two blocks of graphene plates. These graphene blocks are equipped with openings on one side to allow for the flow of electrolyte. Electrodeposited **2** was placed on the anode side and on the cathode side platinum plates were employed, both with a surface area of 1.5 cm^2. A porous Teflon sheet acts as the main separator for electrodes, to avoid unnecessary crossover. Additionally, to prevent leaking from the long period of flow, two Teflon gaskets of 5 cm^2 were placed on both sides of the cell block. A gear pump (March Manufacturing Inc.) was utilized for this stability test because the porous Teflon sheet doesn't provide enough pressure to separate the two flows. Thus, only one pump was implemented to ensure the entire cell will have electrolyte cycled through. The output pump was connected to the lower inlet of the graphene block and an upper outlet was connected into the material storage tank where the electrolyte is.

RESULTS AND DISSCUSSION:

Scheme 1. Immobilization of [2,2′-Bipyridine]-4,4′-bis(diazonium) Rhenium Complex via electrochemical grafting.

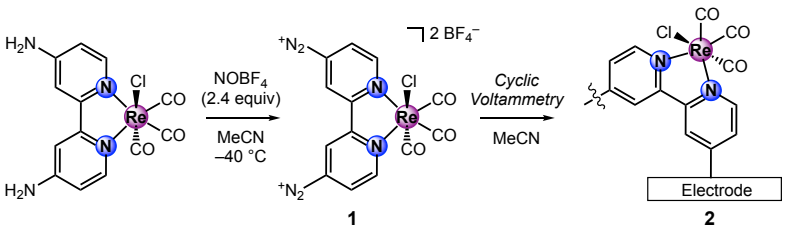

Synthesis of [2,2′-Bipyridine]-4,4′-bis(diazonium) Rhenium Complex. The rhenium [2,2′-bipyridine]-4,4′-diamine complex (Scheme 1) was synthesized according to a metalation procedure reported for the [2,2′-bipyridine]-5,5′-diamine ligand with rhenium(I) pentacarbonyl chloride in a refluxed toluene solution.[12,22] The ^{1}H-NMR spectrum of the rhenium [2,2′-bipyridine]-4,4′-diamine complex in acetonitrile-d_3 displays peaks corresponding to the aromatic protons on the bipyridine backbone at δ 8.34, 7.28, and 6.68 ppm and to the 2H pendant amine protons at δ 5.66 ppm (**Figure S1**).[22] Treatment of [2,2′-bipyridine]-4,4′-diamine complex with nitrosonium tetrafluoroborate (2.4 eq.) in anhydrous acetonitrile at -40 °C caused an instant color change from an opaque yellow solution to deep violet. Anhydrous diethyl ether was used to precipitate an adhesive-dark-purple solid, which was collected via vacuum filtration, and stored in a freezer at -27°C. The rhenium [2,2′-bipyridine]-4,4′-bis(diazonium) complex (**1**) was characterized through ^{1}H and ^{19}F-NMR spectroscopy, UV-Vis spectroscopy, and attenuated total reflectance Fourier transform infrared spectroscopy (ATR-FTIR). The ^{1}H-NMR spectrum of **1** in acetonitrile-d_3 displays three aromatic peaks at δ 9.70, 9.35, and 8.66 ppm with 1:1:1 ratio and assigned to the protons of the bipyridine backbone (**Figure S2**). A notable downfield shift of **1** from the aromatic proton peaks of the rhenium [2,2′-bipyridine]-4,4′-diamine complex at δ 8.34, 7.28, and 6.68 ppm,[22] is due to the electron-withdrawing substituents on the bipyridine. In addition, the absence of the previously assigned pendant amine proton signal, at δ 5.66 ppm,[22] further supports the conversion of the diamine into the diazonium moiety. The ^{19}F-NMR spectrum of **1** in acetonitrile-d_3 displays a peak around δ -150.8 ppm, which is assigned to the tetrafluoroborate anion (**Figure S3**). The ATR-FTIR spectrum of **1** displays a characteristic CO stretch at 2028 cm^{-1}, and two stretching vibrations coalesced within a broad signal at 1918 cm^{-1}, which is characteristic of the *fac*-Re(CO)$_3$Cl species (**Figure S4**).[24,25] An additional stretching vibration resides around 2320 cm^{-1}, which corresponds to a diazonium stretch.[16,26] The UV-Vis spectrum of **1** (0.125 mM in acetonitrile) was collected (**Figure S5**). The spectrum displays two strong absorption peaks at 350 nm and 540 nm. The signals are assigned to a $\pi \rightarrow \pi^*$ bipyridine absorption and to mixed dπ (Re) $\rightarrow \pi^*$ (bpy) metal-to-ligand-charge-transfer (MLCT)/p(Cl) $\rightarrow \pi^*$(bpy) ligand-to-ligand CT (LLCT), referred to as MLLCT,[27,28] respectively (**Table S1**). This characterization clearly indicates the successful synthesis of **1** and that the electronic transitions parallel to that of the *fac*-Re(CO)$_3$Cl species.

A spectroscopic comparison of complex **1** against that of the previously reported [2,2′-bipyridine]-5,5′-bis(diazonium) chlororhenium(I), referred to as 5,5′-(bis)diazonium henceforth, was pursued to elucidate changes in the electronic structure of both monomers. A notable blue shift of ~72 nm and a red shift of ~24 nm occurs for the MLLCT absorption and $\pi \rightarrow \pi^*$ transition of **1**, respectively, when compared to those for 5,5′-(bis)diazonium (**Table S1**). The positioning of the electron-withdrawing substituent N_2^+ in the 5,5′-position causes a stronger shift of electron density away from the electron-rich metal center, thus stabilizing the ligand-based π^* orbital and results in a weaker MLLCT transition. The stabilized π^* orbital phenomenon was also seen in the analogous complex system of [2,2′-bipyridine]-4,4′-bromomanganese(I),[29] and bathchromatic shifts in rhenium tricarbonyl systems with extended conjugation.[30] In contrast, the latter red shift of the $\pi \rightarrow \pi^*$ transition demonstrates the induction effect the electron-withdrawing substituents exert on the bipyridine ligand for **1**. The diazonium group, N_2^+, positioned para to the heteroatom nitrogen extends the conjugation as evident by the longer wavelength of the maximum absorption.[31–33] Similarly, the ATR-FTIR spectra for complex **1** displayed a red shift for the in-phase-symmetric carbonyl stretching frequency from 2033 to 2028 cm^{-1} , when compared to 5,5′-(bis)diazonium (**Table S2**), suggesting that the electron density deficiency is greater for the 5,5′-

(bis)diazonium, as a decrease in the carbonyl stretching frequency can be associated with stronger back bonding donation, and subsequently longer C–O bonds from decreased electron density around the metal center.

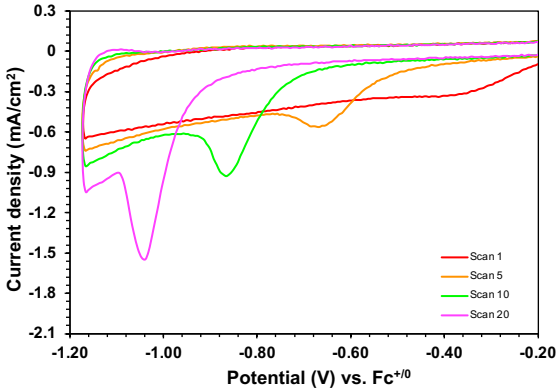

Figure 1. Various electropolymerizations of complex **1** (0.5 mM) onto glassy carbon electrodes via cyclic voltammetry in acetonitrile solutions with 0.1 M $TBAPF_6$ electrolyte to generate films **2**. The scans were performed with a scan rate of ν = 1 V s^{-1} with P_i = -0.2 V and P_s = -1.2 V.

Electropolymerization of [2,2'-Bipyridine]-4,4'-bis(diazonium) Rhenium Complex. Complex **1** was grafted onto substrates of glassy carbon (GC) (**Figure S6**), fluorine-doped tin oxide (FTO) (**Figure S7**), gold (Au) (**Figure S8**), and carbon cloth (CC) (**Figure S9**) electrodes to form grafted films (labeled as **2**) and was subjected to characterization and electrochemical studies. GC was chosen for electrochemical measurements. FTO substrate was chosen for characterization due to the electrode's transparent nature and Au was chosen for its highly reflective nature, making both substrates ideal for spectroscopic measurements. The CC substrate is employed to test the catalytic activity of **2** and can be used as a comparison to the FTO characterization. Cyclic voltammetry (CV) was conducted with an initial potential (P_i) of -0.2 V vs. $Fc^{+/0}$ (all subsequent potentials are referenced to the ferrocene/ferrocenium reversible couple unless otherwise stated), and a switching potential (P_s) of -1.2 V in the presence of 0.5 mM of **1** in an acetonitrile solution with 0.1 M $TBAPF_6$ electrolyte (**Figure 1)**. Previous work by Pinson, Savéant, and their coworkers demonstrated that the successful electrografting of diazonium salts is attributed to the formation of aryl radicals at potentials that do not further reduce to the anion species.[34] The mild P_s of -1.2 V chosen for grafting ensures the anion is not produced. Additionally, no ferrocene standard was added to the medium to avoid the introduction of ferrocene into the grafted polymer matrix. A scan rate of ν = 1 V s^{-1} was used to facilitate uniform film growth and minimize impeding charged trapped species during grafting.[35] The potential window was previously optimized as it can influence the deposition of the diazonium complex.[21] The number of grafted scans applied to generate the modified electrodes, n, varied from n = 1, 5, 10, 20, and so on. Henceforth, the substrates will be referred to as **X**-Y-n, where **X** are the grafted films **2**, and Y is the substrate of interest (e.g. GC), and n is the number of grafted scans. After deposition, the electrodes were thoroughly rinsed with acetonitrile and acetone to remove any weakly absorbed species. During the electropolymerization of **1** into **2,** an irreversible broad cathodic feature appears around -0.40 V for **2**-GC-1 (**Figure 1**). As n increases, this feature is shifted cathodically to potentials of -1.05 V (for **2**-GC-20). The prior broad feature is attributed to a previously assigned one-electron bipyridine reduction, and consequently, a reduction of the diazonium substituent.[12] This reduction feature corresponds to the formation of aryl radicals near the surface of the electrode and subsequent release of N_2, common for electrochemical reduction of diazonium species.[16,36] The

latter reduction feature at -1.05 V for **2**-GC-20 is attributed to a blocking effect of the deposited layer as the charge transport to the substrate becomes increasingly barred, hindering further reduction.[36] This peak increase and cathodic shift are both indicative of successive grafting layers of molecular diazonium species.

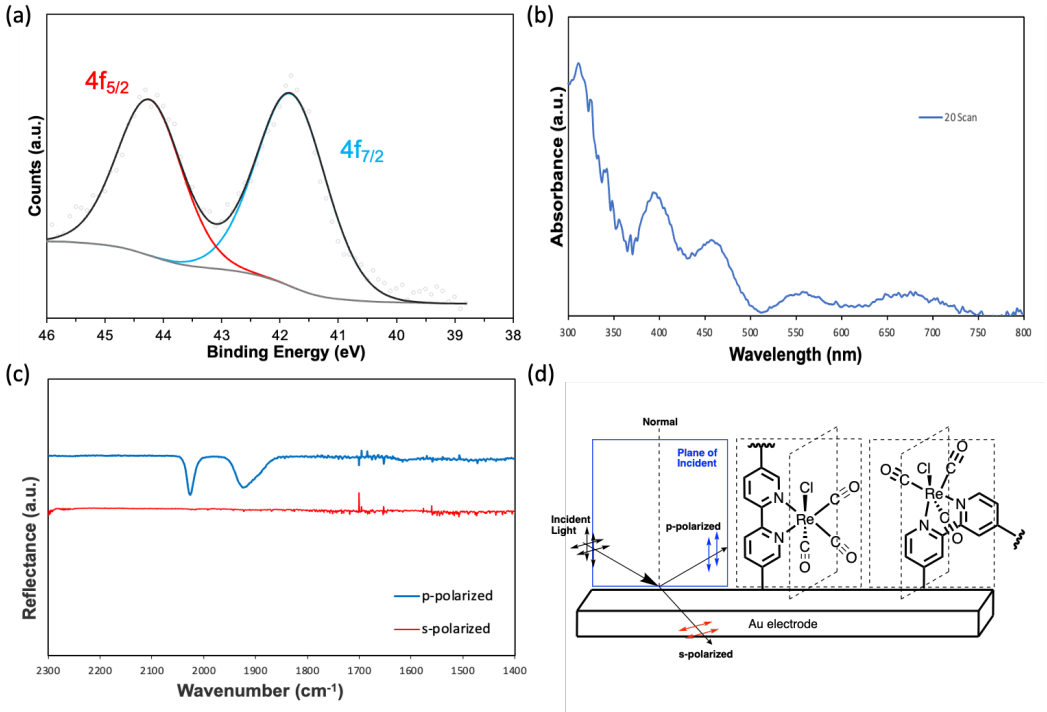

Figure 2. (a) High-resolution Re 4f XPS spectrum for a modified **2**-FTO-10 electrode. (b) UV−vis absorption spectrum measured for a modified **2**-FTO-20 substrate. (c) Polarized IRRAS results measured for a modified **2**-Au-20 substrate under both p- (blue trace) and s- (red trace) polarization. (d) S-, p-polarization, and fixed carbonyl stretching frequency planes of grafted [2,2′-bipyridine] rhenium(I) complexes based on the orientation to the plane of incident.

Characterization of Grafted Films. To characterize the modified electrodes, the substrate was submitted to a series of spectroscopic measurements of UV-Vis, infrared-reflection absorption spectroscopy (IRRAS), scanning electron microscopy (SEM), and X-ray photoelectron spectroscopy (XPS). After grafting and rinsing, the **2**-FTO-10 and **2**-CC-10 modified electrodes were analyzed by XPS. The survey XPS displays distinct signals corresponding to elements of 1s C, 1s N, 1s O, 1s F, 2p Cl, 2p P, 1s B, and 4f Re (**Figure S10b**). The rhenium 4f region displays two peaks at 44.3 and 41.8 eV, corresponding to the Re $4f_{5/2}$ and $4f_{7/2}$, respectively (**Figure 2a** and **Table S3**). Depending on the substrate, the signals are similar in binding energy (BE) with signals around 41.8 eV corresponding to Re $4f_{7/2}$ for both **2**-FTO-10 and **2**-CC-10 (**Figure S11** and **Table S3**). Interestingly, the high-resolution Sn 2p region displays two peaks at 495.6 and 487.1 eV, and a satellite peak at 497.6 eV for **2**-FTO-10 (**Figure S12** and **Table S3**), which were assigned to the Sn $3d_{3/2}$ and $3d_{5/2}$, and a plasmon-loss of the substrate, respectively. The appearance of Sn core levels indicates that film thickness does not exceed the XPS sample depth (~5 – 10 nm) for films loading up to n = 10. The satellite feature represents the energy loss of the fraction of photoelectrons from collective excitations during XPS excitation.[37] Additionally, the high-resolution Cl 2p region displays signals at 197.8 and 199.4 eV for **2**-CC-10, which correspond to $2p_{3/2}$ and $2p_{1/2}$, respectively (**Figure S13b** and **Table S3**). The use of FTO electrodes displays a

similar signal at 198.2 eV, corresponding to the $2p_{1/2}$, which is a 1.2 eV shift in binding energy (**Figure S13a**). This shift is due to fluorine interstitial defects of FTO on soda lime glass, where XPS analysis of this substrate has been shown to display plasmon-loss components of core-level lines.[37] This phenomenon is also present when comparing the survey spectra between the **2**-FTO-10 and **2**-CC-10 (**Figure S10**), in which inelastic scattering of electrons is displayed at higher binding energies for **2**-FTO-10 (**Figure S10a**). Furthermore, the F 1s displays a small satellite feature at higher binding energies in the **2**-FTO-10 film, likewise supporting the plasmon-loss associated with the surface of FTO electrodes (**Figure S14a**). This phenomenon is also the reason for the appearance of only one F 1s signal for **2**-FTO-10. Correspondingly, the F 1s region exhibits two peaks present at 685.9 and 688.8 eV for **2**-CC-10 (**Figure S14b** and **Table S3**). The prior is assigned to an F 1s signal for the ionic species of BF_4^-,[38] whereas the latter F 1s signal is assigned to the PF_6^- due to the higher shift in binding energy; a result of the higher electronegativity of phosphorus. Moreover, the P 2p region for the **2**-FTO-10 displays three signals at 133.8, 134.7, and 139.0 eV. The first two signals correlate to the $2p_{3/2}$ and $2p_{1/2}$ energy levels, respectively, for the PF_6^- anion (**Figure S15a** and **Table S3**). The latter is the Sn 4s signal, captured within the spectrum window of P 2p. Also, the B 1s for **2**-FTO-10 corroborates the appearance of the BF_4^- anionic species (**Figure S15b**). This XPS analysis is consistent with the trapping of redox species within the film matrix during electropolymerization of **1** to generate films **2** (vide infra).[21,39,40] Lastly, an examination of the C 1s region of **2**-CC-10 displays two signals at 284.7 and 286.2 eV, both corresponding to polymer binding energies of C-C and C-N groups, respectively (**Figure S16** and **Table S3**).[41] An additional broad signal present at ~292.9 eV is assigned to a $\pi \rightarrow \pi^*$ shakeup satellite feature, a signal that is associated with an electronic transition in conjugated unsaturated bonding.[42–44] This XPS characterization demonstrates that the structural integrity is retained upon electropolymerization, the substrate chosen has minimal influence on the electronic communication of the grafted complex, the trapping of anionic species within the polymer matrix, and the conjugated connectivity of the tethered complex.

Comparisons of XPS characterization of the grafted analogue, 5,5′-ReBpy, with that of **2** were done to provide information on how the structural electronic integrity is changed as a function of the tethering position of the bipyridine backbone (**Table S3**). The binding energy (BE) of the high-resolution Re 4f region demonstrates the Re $4f_{7/2}$ signal for the grafted films **2**-FTO-10, and 5,5′-ReBpy onto FTO is within the expected literature value for a +1 oxidation state.[45] Additionally, the Re $4f_{5/2}$ and $4f_{7/2}$ peaks for **2**-FTO-10 are shifted ~0.8 eV higher in BE when compared to 5,5′-ReBpy. Moreover, the Cl $2p_{3/2}$ peak for complex **2**-CC-10 exhibits a BE shift of ~0.8 eV when compared to 5,5′-ReBpy. This shift towards higher BE is a result of the 4,4′-tethering of the bipyridine backbone which imparts a change in the growth morphology that results in a reduction of electron density away from the Re center, thus the Re center is more electron deficient when compared to the 5,5′-tethering in 5,5′-ReBpy. The appearance of signals in the P 2p and F 1s demonstrates the entanglement of the PF_6^- and BF_4^- anions within the polymer matrix of both films, **2** and 5,5′-ReBpy.

UV-Vis measurements were performed on the **2**-FTO-20, using FTO as a transparent substrate (**Figure 2b** and **Table S1**). The spectrum displays two strong absorption peaks at 314 and 394 nm, along with two broad absorption features at 560 and 680 nm, and intermediate absorption at 450 nm. The high-intensity signals at 314 and 394 nm are assigned to the intraligand $\pi - \pi^*$ transitions (IL) of the polymer backbone,[46] and the lower-intensity broad signals at 560 and 680 nm are assigned to mixed $d\pi$ (Re) $\rightarrow \pi^*$ (bpy) metal-to-ligand-charge-transfer (MLCT)/p(Cl) $\rightarrow \pi^*$(bpy) ligand-to-ligand CT (LLCT), referred to as MLLCT.[27,28] It is known, from time-

dependent density functional theory, that the lowest energy optical transitions are representative of MLCT.[47,48] Additionally, halide ligands induce delocalization of frontier orbitals that is better described as electron density transferred from the whole $Re(CO)_3$ fragment, rather than just from Re.[27] Similarly, the contribution of interligand CT between adjacent immobilized bipyridine molecules cannot be ruled out.[49,50] These absorption features have also been observed on FTO-modified electrodes with lower grafted scans, **2**-FTO-10 (**Figure S17**). The absorption at 450 nm corresponds to the contribution of the electronic excitation of a possible Re-Re dimer species during the electropolymerization of complex **1**. These UV-Vis absorption signals match well the values of the previously reported peaks for the Re-Re dimer.[24,51,52]

The UV-Vis results of **2**-FTO-10 were compared with that of the analogous grafted 5,5′-ReBpy onto FTO to determine how the electronic excitations change as a function of the tethering position. The IL transition for **2** is blue-shifted by ~22 nm, from 336 to 314 nm (**Table S1**). However, examining the MLLCT transition of **2**, there is a notable red shift of ~64 nm from 496 to 560 nm. This decrease in MLLCT band energy contrasts with the blue-shifted UV-Vis of the MLLCT of **1**. The prior shift is indicative of a decrease in conjugation,[53] whereas the latter displays a decreased MLLCT band energy where the tethered 4,4′-positioning induces a lowering of the LUMO of π^*(bpy). The decreased MLLCT band energy for **2** is a phenomenon common for Bpy derivatives with electron-withdrawing groups.[54] The decrease in MLLCT band energy and decrease in conjugation is due to unpredictable growth of **2** and possible dimer formation. These UV-Vis results, in conjunction with the XPS characterization, demonstrate the electronic environment and structural integrity of the rhenium bipyridine moiety is retained after electropolymerization and that the electronic excitations can change as a function of the tethering of the bipyridine backbone.

Additional characterization of IRRAS was performed as a surface-sensitive technique to observe the previously documented three rhenium *fac*-$(CO)_3$ stretch modes of in-phase symmetric a'(1), anti-symmetric a", and out-of-phase symmetric a'(2) stretches.[55,56] This study was conducted on modified grafted Au electrodes, as Au possesses high reflectance and high conductivity characteristics. The IRRAS spectrum for a modified **2**-Au-20 electrode displays two stretching frequencies: a sharp feature at 2026 cm^{-1}, and a broad frequency at 1922 cm^{-1} (**Figure 2c** and **Table S2**), which are characteristic of CO stretching frequencies. The sharp feature at 2026 cm^{-1} is assigned to the a'(1) stretching frequency, whereas the broad frequency at 1922 cm^{-1} is assigned to the overlapping a" and a'(2) symmetry stretches, respectively.

Moreover, comparisons of the IRRAS spectra of the immobilized films **2** can be made with that of **1**, and that of the analogous 5,5′-ReBpy complex to probe how electronic communication changes upon electropolymerization and as a function of positional immobilization (**Table S2**). Upon electropolymerization of **1** to **2** on Au electrodes, only a slight blue shift of 2 cm^{-1} is observed for the sharp a'(1) feature, signifying that there is little to no change in the electronic structure upon electropolymerization. Correspondingly, **2** is red-shifted by 4 cm^{-1} for the a'(1) stretching mode, when compared to 5,5′-ReBpy. This data contrasts with what is observed for UV-Vis and XPS characterization, as **2** should possess blue-shifted stretches when compared to 5,5′-ReBpy. This discrepancy may be due to the sample penetration depth of IRRAS and the long-range order of 5,5′-ReBpy films. At a 56º angle of incidence, and the wavenumber of interest (~2000 cm^{-1}), the sample penetration depth would be limited to shallow sampling depths. Additionally, it has been previously reported that immobilized ReBpy species can possess strong intermolecular π-π stacking interactions that can induce a blue-shift for the a'(1) stretching mode.[57–59] Similarly, the 5,5′-ReBpy films have previously been reported to have a long-range order film growth.[21] Due to

the growth morphology of **2** (vide infra), it is possible that the IRRAS measurement would excite a larger concentration of the upper-layered immobilized 5,5′-ReBpy species, therefore elucidating larger contributions of intermolecular interactions than those observed for **2**, and thus, resulting in a higher wavelength frequency absorption for 5,5′-ReBpy.

To probe the long-range growth morphology of the film, polarized IRRAS studies were carried out with a ZnSe polarizing lens. In previous studies of monolayer films, the determination of molecular orientation relies on two methods: (1) Determining spectral intensity with p-polarization at several angles of incident or (2) with both p-polarization (parallel to the plane of incident) and s-polarization (perpendicular to the plane of incident) radiation at a single angle of incident (**Figure 2d**).[60,61] The latter radiation was chosen as a proxy for the qualitative determination of the relative orientation of the immobilized species. Quantitative determination is beyond the scope of this work and the reader should be directed to the references above for a more in-depth analysis method. The degree of polarization was quantified using the ratio of the peak height (ΔR) for a'(1) carbonyl stretching mode at 2026 cm^{-1} under p- and s-polarization ($\Delta R_p/\Delta R_s$). Examining the spectra collected for the modified **2**-Au-20 electrode, the p-polarization displays increased absorption for the assigned carbonyl stretches ($\Delta R_p/\Delta R_s = 40$), whereas the s-polarization shows little to no absorption ($\Delta R_s/\Delta R_p = 0.03$). This result is in contrast to that observed for the 5,5′-ReBpy analogue, for which the s-polarization displays increased absorption.[21] Using bonding considerations, these results indicate that the C≡O ligand in **2** is positioned parallel to the plane of incident, whereas the C≡O in the previously reported grafted 5,5′-ReBpy complex is positioned perpendicular to the plane of incident.[21] Based on these results, a relative comparison can be made on the orientation of the immobilized species. The strong p-polarization dependence observed for the stretching modes of **2** indicates horizontal film growth (the film branches outwards as opposed to generating linear orientations). This long-range morphology differs from that of the previously reported grafted 5,5′-ReBpy complex, where the immobilized system displayed a larger polarization dependence for the vertical growth orientation.[21] The qualitative orientation of **2**-Au-20 demonstrates the drastic change in growth morphology from a slight change in the tethering position from the 5,5′- to 4,4′- position of the bipyridine backbone. Additionally, this change in surface orientation for **2** opens the possibility of Re-Re dimer formation and strong π-π stacking interactions.[62–64]

To further probe the surface morphology of the anchored films, SEM image acquisitions were performed with the modified **2**-Au-**20** electrode. As illustrated in **Figure S18a**, the film morphology possesses overall smooth surface coverage with small aggregation formations. Regions of brighter areas are a result of the backscattering of heavier elements captured in the through lens detector (TLD) of the instrument, suggesting the formation of micro-meter clusters of rhenium. Furthermore, a gold electrode was acid-etched prior to electropolymerization (**Figure S18b**). Signified by the appearance of a minor defect crack present on the surface of the Au electrode, the immobilized film bridges over the surface of the defects and creates smooth features, further supporting the horizontal growth (with respect to the surface normal) of **2**. The appearance of micro-clusters increased as the roughness of the surface increased due to acid-etched preparation.

Electrochemistry of Grafted Films. Once the characterization of the grafted electrodes was complete, cyclic voltammetry was employed for grafted films of **2**-GC-1 to **2**-GC-20 loadings (**Figure S19**). The CVs were performed with P_i = open circuit potential (OCP), an anodic switching potential of 0.8 V (P_a = 0.8 V), followed by a cathodic switching potential of -2.6 V (P_c = -2.6 V).

Each scan was performed with a scan rate of ν = 100 mV s^{-1}. All measurements were performed on grafted electrodes, rinsed vigorously with acetonitrile and acetone; and complex **1** was not present in the medium of analysis. Under N_2 atmosphere, an irreversible cathodic feature is observed at potentials around -1.00 V for each of the grafted films (**Figure S19**), which is attributed to the discharge of charge-trapped electrolyte, that accumulated during the electropolymerization process; a feature common in conducting polymer matrices with metal complexes.[21,39,40] Also under N_2 atmosphere, a quasi-reversible cathodic feature occurring around -1.80 V for each loading is attributed to previously assigned two ligand-based reduction events converging into a single broad two-electron reduction.[12] In addition, the modified electrodes each displayed a decrease in the current density upon the second CV scan, before stabilizing with subsequent CV cycles (**Figure S20**). This behavior is attributed to n-doping of the bipyridine backbone upon polarization.[65] For this reason, subsequent CV analysis was done up to two cycles. Additionally, an irreversible oxidation event for **2** appears after the first cycle of CV scans at -0.2 V (**Figure S20**). This signal is attributed to the oxidative cleavage of the Re-Re dimer to form two independent Re(I) fragments.[62] This electrochemical response further provides evidence of dimer formation.

To determine the reactivity of films **2** onto GC, each modified substrate was subjected to CV studies under a saturated CO_2 atmosphere (**Figure S19**). For each film, there was a loss of reversibility from switching from N_2- to CO_2-saturated solutions, as well as a subsequent increase in the current density, thus signifying that a reaction is occurring. For each loading, the catalytic feature increased in current density from **2**-GC-1 up to **2**-GC-10, followed by a decrease in the current density as the number of scans n increased to 20 in **2**-GC-20. These studies indicate that thicker films display a decreased catalytic activity, which could be a result of inhibited substrate diffusion for higher-loading films as indicated for **2**-GC-20. This study indicates that films with n = 10 scans display the optimal catalytic activity for the GC electrode. An additional UV-Vis measurement was performed with **2**-FTO-10, before and after the CV studies under a CO_2-saturated solution and displayed little to no losses in the intensity for the absorption peaks (**Figure S21**).

Furthermore, electrochemical impedance spectroscopy (EIS) measurements were conducted in CO_2-saturated acetonitrile solutions with 0.1 M $[NBu_4][PF_6]$ to elucidate the charge transport properties based on the thickness of the films deposited. The Nyquist plot displays the response of high frequencies to low frequencies (**Figure S22**). This plot serves as a proxy to find the solution resistance (R_s) at high frequencies. The semi-circle at low frequencies provides both the charge-transfer resistance (R_{ct}) and R_s. At the open circuit potential (OCP), resistance is similar across each of the films, except for **2**-GC-10 which displays a lower resistance (**Table S4**) when compared to other catalyst loadings. An increase in the magnitude of the potential applied results in an overall decrease in R_{ct} for each film. Examination of each response at -2.4 V displays R_{ct} values of 1.97×10^5, 8.79×10^4, 1.27×10^5 ohms for **2**-GC-5, **2**-GC-10, and **2**-GC-20, respectively. When comparing impedance, a noticeable decrease in the R_{ct} occurs from **2**-GC-5 to **2**-GC-10, followed however by a further increase in the R_{ct} for **2**-GC-20. This study indicates that **2**-GC-10 displays enhanced charge transfer properties, further demonstrating the optimal film thickness to be **2**-GC-10 on GC substrates.

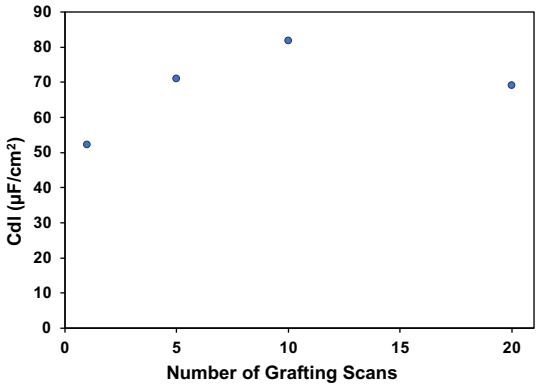

Figure 3. Cdl of glassy carbon modified electrodes as a function of the number of grafting scans.

Next, double-layer capacitance (C_{dl}) was used as a substitute for determining the electrochemically active surface area (ECSA) at the surface of the deposited films. C_{dl} measurements were performed within a 100 mV window and at a non-Faradaic capacitance region (**Figure S23**). If the change in current density ($\Delta J = J_{anodic} - J_{cathodic}$), centered at OCP, is plotted as a function of the scan rate, the result is a slope equal to the C_{dl} (**Figure S24**). This analysis is derived from the knowledge that the double-layer charging current is equal to the product of scan rate and the C_{dl}.[66] There is a linear increase in ECSA from **2**-GC-1 to **2**-GC-10, but saturation is reached and a subsequent decrease in ECSA occurs for **2**-GC-20 (**Figure 3**). This behavior indicates that the optimal catalyst loading is reached for **2**-GC-10, based on the highest ECSA of $C_{dl} = 81.8\ \mu F/cm^2$. An optimized catalyst loading ($\leq n = 10$) was also observed for the 5,5′-ReBpy analogue.[21] This evidence warranted the exploration of other substrates for CO_2 reduction.

Electrocatalysis of Grafted Films. Catalyst loadings higher than n = 10 on the modified glassy carbon electrodes displayed mass transportation limitations, and unfortunately the GC electrodes with this low catalyst loading (n = 10) do not generate enough products for quantification. Interested in improving this mass transport limitation, further electrochemical analysis was carried out on carbon cloth (CC) modified electrodes to test the activity in terms of selectivity and stability of the immobilized 4,4′-ReBpy system. CC was chosen as a substrate due to previously reported high catalytic activity (FE_{CO} = 99% and TON ~290,000) for the analogous immobilized 5,5'-ReBpy,[67] low electrical resistance, low cost, and large surface area.[68]

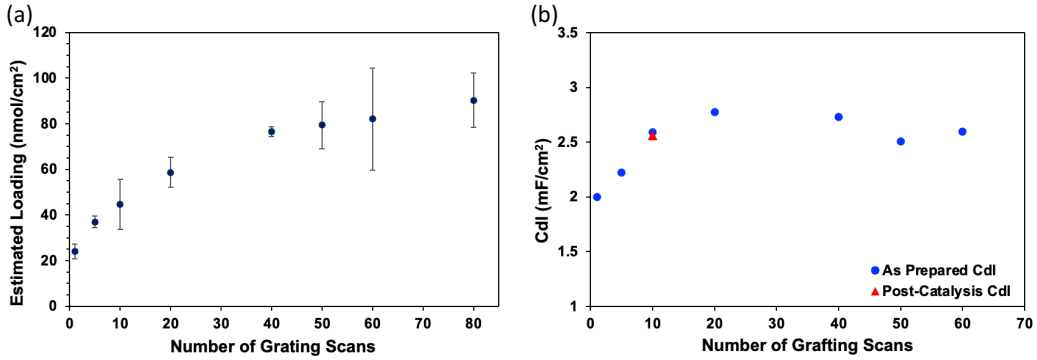

Figure 4. (a) Catalyst loading of carbon cloth electrodes **2** as a function of the number of grafting scans and referenced to the geometrical surface area of 1.5 cm^2. (b) Cdl of deposited films as a function of the number of grafting scans on carbon cloth performed before (blue) and after (red) CPE.

Interested in the optimization of the catalyst loading on CC electrodes, inductively coupled plasma optical emission spectroscopy (ICP-OES) analysis and double-layer capacitance (C_{dl}) measurements were performed to determine the catalyst loading and provide an estimate of the ECSA of the CC modified electrodes as a function of the number of electrodeposition CV scans (**Tables S5** & **Figure 4**). For ICP-OES measurements, the films were digested through overnight sonication in 2 mL of concentrated nitric acid and subsequently diluted to 100 mL with deionized (DI) water. The C_{dl} measurements were conducted in a solution of 0.1 M $[NBu_4][PF_6]$ in acetonitrile and with a geometrical surface area of 1.5 cm^2 (**Figure S25 & S26**). The analysis of ICP-OES revealed a linear correlation between the number of grafting scans and catalyst loading on **2**-CC substrates, ranging from **2**-CC-1 to **2**-CC-20 (**Figure 4a**). An increase from **2**-CC-20 to **2**-CC-40 resulted in a saturation of catalyst loading, with subsequent deposition yielding a minimal increase. The highest catalyst loading achieved was 90.3 ± 12 nmol/cm^2 for the **2**-CC-80 sample. Catalyst loadings of **2**-CC-10 to **2**-CC-80 are higher, but in line with surface coverage of analogous immobilized complexes.[68,69] This is attributed to the increased surface area of CC over GC supports and the potential formation of intermolecular π-π stacking interactions at higher catalyst loadings.

Interestingly, the C_{dl} measurements also outline a linear increase in the ECSA as the loading increases from **2**-CC-1 to **2**-CC-10, with a saturation point being reached before **2**-CC-20 (**Figure 4b**). Although subsequent CV deposition scans result in higher loading, it does not linearly correlate with the ECSA. Once a catalyst loading of 44.6 ± 11 nmol/cm^2 is reached for n = 10, there is a saturation in the ECSA with higher loadings only resulting in a negligible increase (<110 μF/cm^2 deviation), suggesting that the optimal loading is already reached by **2**-CC-10. Comparatively, the analogous immobilized 5,5'-ReBpy on CC deposits a lower amount of overall catalyst during electropolymerization as 5 scans resulted in 3.2 nmol,[67] whereas **2**-CC-1 has already reached a deposition of 23.9 ± 3.2 nmol/cm^2 after 1 scan. This discrepancy in electrodeposition can be explained by the difference in the long-range growth morphology of the respective films. Due to the tethering position of **2**, the films grow horizontally with respect to the surface normal of the substrate (vide supra). This surface configuration opens the possibility to Re-Re dimer formation and π-π stacking interactions that would result in denser films.[62–64] As a result, a lower ECSA is observed for thicker films as dimer and π-π stacking interactions could lead to the possible formation of aggregates as thicker films may block access to the buried active sites beneath the uppermost film layers.[70,71]

To further elucidate the degree of aggregation at higher catalyst loadings, p-polarized IRRAS measurements were carried out with a ZnSe polarizing lens and with samples of varying catalyst loadings from **2**-Au-1 to **2**-Au-20 (**Figure S27**). An apparent blue shift of ~ 4 cm^{-1} of the symmetric stretching vibration a'(1) from **2**-Au-1 to **2**-Au-20 films is observed. Correspondingly, Zanni and coworkers previously used 2D IR, FTIR experiments, and quantum-chemical calculations to demonstrate intermolecular coupling between ReBpy dyes tethered on the interface of TiO_2 at the 4′- and 4,4′-position of the bipyridine, which induced a blue-shift for the symmetric stretching vibration a'(1) as ReBpy aggregation increased.[57] Indeed, a similar trend is observed here for **2**, alluding to the existence of surface ReBpy aggregates that arise from intermolecular interactions and dimer formation as the catalyst loading is increased.[57–59] A consideration of the electrochemistry of **2**-CC under catalytic conditions would adequately elucidate the effect of this increased catalyst loading for CO_2 reduction.

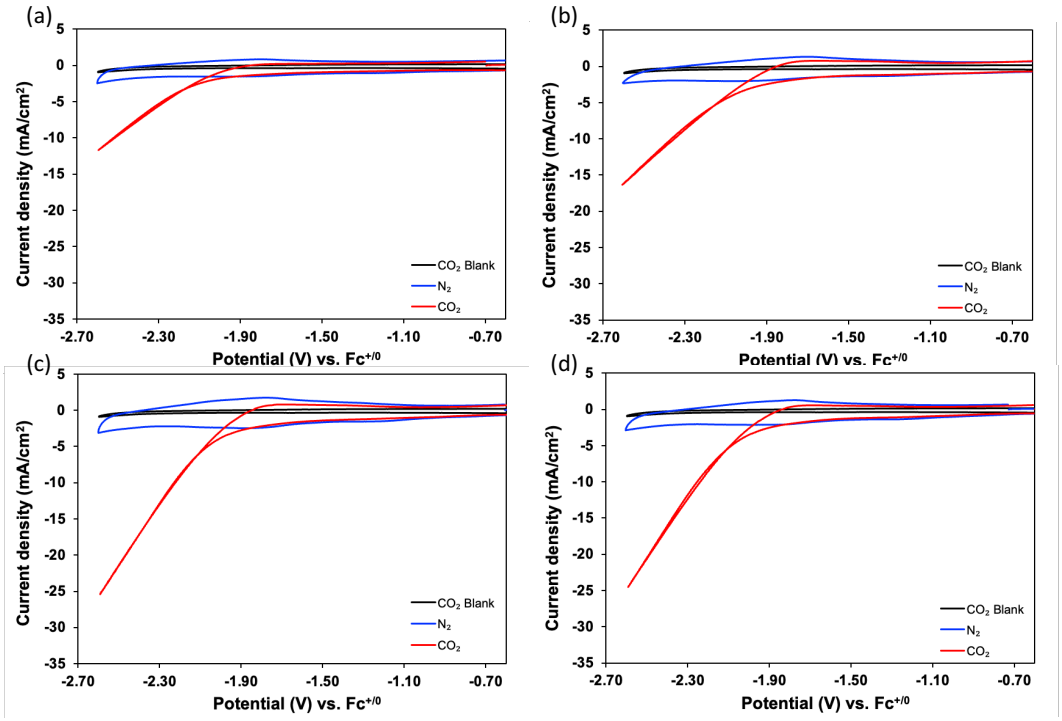

Figure 5. CVs of the grafted films on carbon carbon in acetonitrile solution with 0.1 M $TBAPF_6$ electrolyte under N_2 atmosphere (blue), and in an atmosphere of CO_2 (red). The measurements were performed on (a) **2**-CC-1, (b) **2**-CC-5, (c) **2**-CC-10, (d) **2**-CC-20. Additional control experiments were performed for glassy carbon electrodes under 1 atm of CO_2 (solid black).

To determine the activity of **2**-CC based on the catalyst loading, CVs were employed for grafted films of **2**-CC-1 to **2**-CC-20 (**Figure 5**). The CVs were performed under a saturated N_2 – or CO_2–atmospheres with 0.1 M $[NBu_4][PF_6]$ and P_i = OCP, P_a = 0.8 V, and followed by a cathodic switching potential of P_c = -2.6 V. Each scan was performed with a scan rate of ν = 100 mV s^{-1}. Substituting an N_2-saturated environment with CO_2-saturation, a sharp increase in the current density is observed for all the grafted complexes. The catalytic onset potential occurs around -1.76 V for each of the respective loadings. The lowest loading of **2**-CC-1 exhibits a maximum current density of -11 mA/cm^2. Furthermore, a gradual increase in current density is observed as the catalyst loading is increased from 23.9 ± 3.2 nmol/cm^2 to 58.7 ± 6.5 nmol/cm^2 (**2**-CC-1 – **2**-CC-20), with a maximum current density of -25 mA/cm^2 achieved for **2**-CC-10. A trace cross-over event occurred within the potential range of -2.12 to -2.14 V for all loadings, which indicates a species generated through reduction, that is oxidized at potentials more positive than the initial reduction event of **2**. Although the CV results display a gradual increase in current density throughout the loadings, **2**-CC exhibited mass transport limitations for catalyst loadings greater than 44.6 ± 11 nmol/cm^2 ($n \geq 10$).

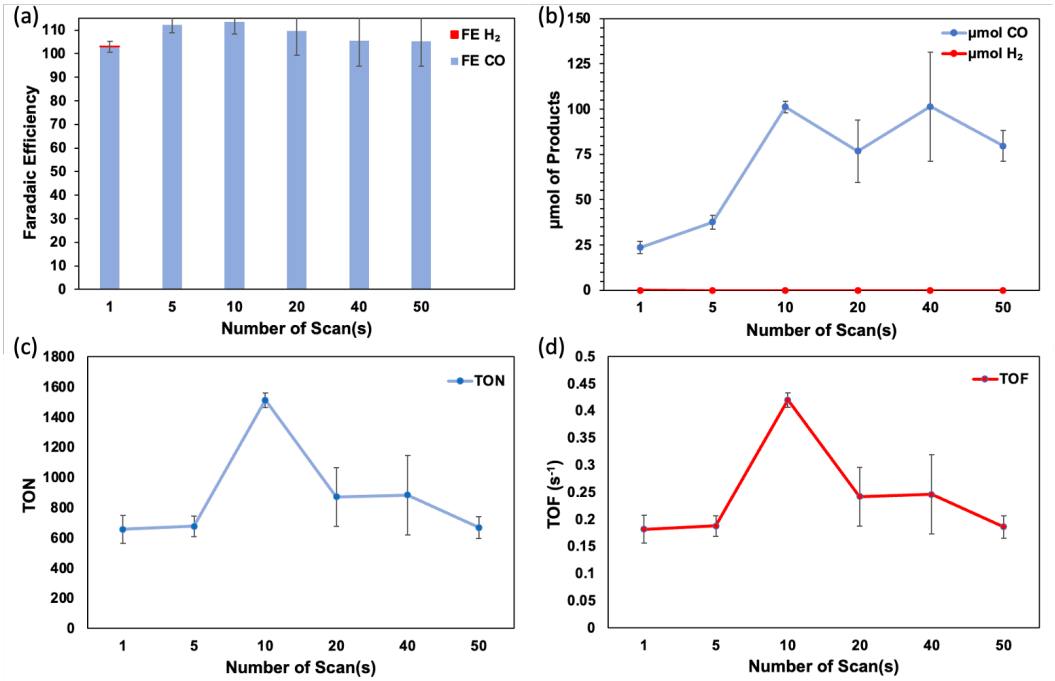

Figure 6. a) Controlled potential electrolysis (CPE) faradaic efficiency results as a function of the number of scans. (b) Amount of the products generated from 1 hr CPE. (c) TON and (d) TOF results of 1 h CPE based on ICP-OES bulk loading. Conditions: each electrolysis was performed at -2.4 V for 1 hr, under H-cell conditions, and in a CO_2-saturated 0.1 M $TBAPF_6$ electrolyte acetonitrile solution.

A series of controlled potential electrolysis (CPE) experiments were conducted with a solution of 0.1 M $[NBu_4][PF_6]$ in acetonitrile and a chosen potential of -2.4 V to optimize the catalytic performance based on catalyst loading (**Figure 6** & **Table 1**). First, a control experiment was performed with the bare substrate, at an applied potential of -2.4 V, and under a CO_2-saturated environment resulting in only 480 mC of charge passed and 0.23 µmol of CO produced (**Table 1**). Following CPE experiments with films **2,** a superior selectivity for CO was displayed across all catalyst loadings with >99 % FE_{CO} and <1% FE_{H2} (**Figure 6a**). All CPE trials resulted in trace amounts of H_2. The turnover number (TON_{CO}) and turnover frequency for CO production (TOF_{CO}) remained nearly constant for lower catalyst loadings of ≤ 37.0 nmol/cm^2 ($n \leq 5$). Correspondingly, at higher catalyst loadings $\geq 58.7 \pm 6.5$ nmol/cm^2 ($n \geq 20$), the TON_{CO} and TOF_{CO} subsequently decreases, while the amount of CO generated remained constant or slightly decreased (**Table 1**). Moreover, the catalytic performance appears to follow a volcano-type trend where saturation is reached at loadings of 44.6 nmol/cm^2 ($n = 10$) and achieved a TON_{CO} of 1513 and a TOF_{CO} of 0.4 s^{-1} (**Figure 6c**). Even in the presence of no added Brønsted acid source, this represents a catalytic improvement of almost three orders of magnitude when compared to the TON_{CO} of the homogeneous rhenium [2,2′-bipyridine]-4,4′-diamine complex (TON_{CO} = 1.6 with a catalyst concentration of 40 µmol).[22] The immobilized complex appears to reach an optimal surface arrangement for loadings of 44.6 nmol/cm^2 ($n = 10$), with a decrease in the CO_2 reduction efficiency as the catalyst loading is further increased. Considering the C_{dl} measurements (**Figure 4b**) of the **2**-CC samples and the IRRAS p-polarized measurements of each **2**-Au samples (**Figure S27**), a possible explanation for the decreased CO_2 reduction efficiency at high catalyst loadings can be attributed to the formation of aggregations that can block access to the underneath film active sites,[72] resulting in inefficient catalysis at higher catalyst loadings.

Table 1. Summary of catalytic CO_2 reduction performance of **2**-CC-1 to **2**-CC-50 measured at -2.4 V.

Sample	Loading ($nmol/cm^2$)	Charge Passed (C)	CO Produced (μmol)	TON_{co}	TOF_{co} (s^{-1})	FE_{co} (%)
Blank	–	0.48	0.23	n/a	n/a	9.1
1 Scan	23.9(3.2)	4.4(0.5)	23.6(3.3)	657(92)	0.2(0.03)	>99(2.4)
5 Scan	37.0(2.7)	6.5(0.5)	37.6(3.7)	668(68)	0.2(0.02)	>99(3.3)
10 Scan	44.6(11)	17.2(0.2)	101.3(3.2)	1513(48)	0.4(0.01)	>99(5.2)
20 Scan	58.7(6.5)	13.7(4.3)	76.8(17)	872(196)	0.2(0.05)	>99(10)
40 Scan	76.5(2.2)	18.3(4.6)	101.4(30)	884(263)	0.3(0.07)	>99(11)
50 Scan	79.3(10)	14.6(0.1)	79.7(8.7)	670(73)	0.2(0.03)	>99(11)

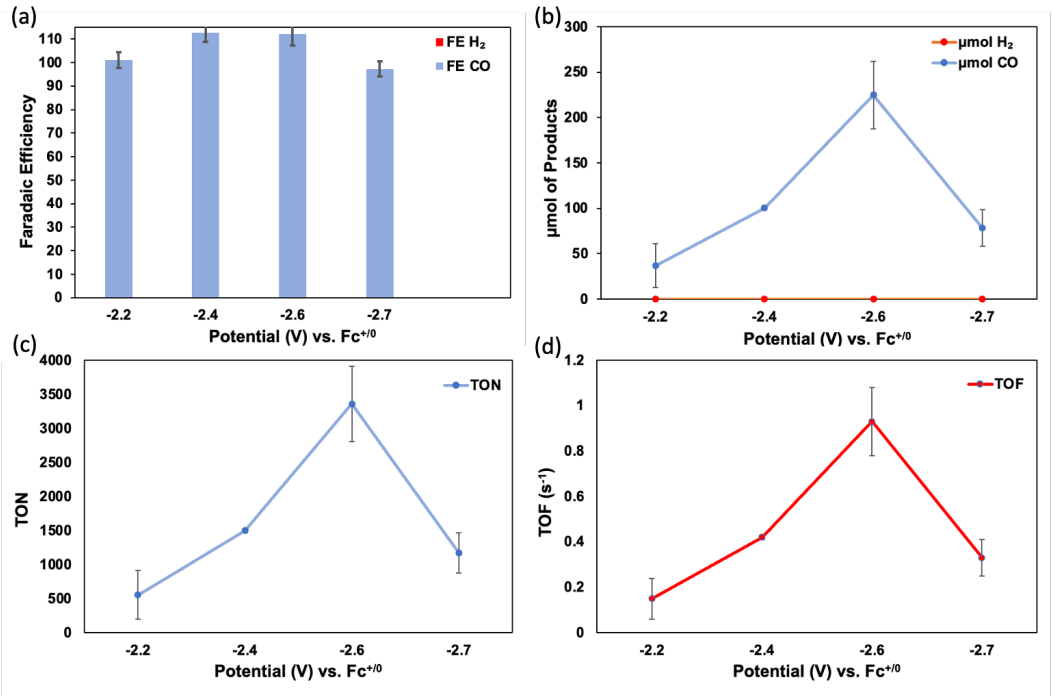

Figure 7. Summary of the results determined from controlled potential electrolysis (CPE) studies performed at a specified potential for 1 h, under 1 atmosphere CO_2, no added proton source, and under H-cell conditions in acetonitrile solutions with 0.1 M $[NBu_4][PF_6]$ supporting electrolyte. (a) CPE faradaic efficiency results as a function of the applied potential. (b) Amount of the products generated from 1 hr CPE. (c) TON and (d) TOF results of 1 h CPE based on ICP-OES bulk loading.

After catalyst loading optimization, the catalytic performance was investigated as a function of the CPE applied potential. An additional control experiment was performed with **2**-CC-10 at an applied potential of -2.6 V, and under an N_2-saturated environment, which resulted in

610 mC of charged passed, < 1 μmol of CO, low TON_{CO} and TOF_{CO} (**Table S6**). Both control experiments imply that there is minimal to no contribution from the bare substrate or from the liberation of CO to the overall catalytic performance of **2**. **2**-CC-10 demonstrated excellent selectivity for all potentials applied with a FE_{co} > 99% (**Figure 7a**). The application of potentials from -2.2 to -2.6 V resulted in an overall increase in activity as the TON_{CO} increased from 552 to 3359, TOF_{CO} increased from 0.2 to 0.9 s^{-1}, and the amount of CO produced increased from 37 to 225 μmol of CO (**Table S6 & Figure 7**). However, the application of larger overpotentials of -2.7 V resulted in a subsequent decrease in the activity. From this, the optimal applied potential was determined to be -2.6 V.

Correspondingly, comparisons of the catalytic activity of **2**-CC-10 can be made with that of the optimal immobilized 5,5'-ReBpy on CC.[67] At higher potentials of -2.7 V, 5,5'-ReBpy produces 581 μmols of CO with larger TON_{CO} and TOF_{CO} values, whereas **2**-CC-10 produces only 78 μmols of CO. Contrastingly, lower applied potentials, of less than -2.3 V, resulted in the production of 6.0 and 36.9 μmol of CO for 5,5'-ReBpy and **2**-CC-10, respectively. However, 5,5'-ReBpy displayed higher TOF_{CO} of 0.5 s^{-1} and TON_{CO} of 1847. This data suggests that 5,5'-ReBpy is more efficient at CO_2 reduction with lower catalyst loadings. An explanation for this can be rationalized by the nature of the growth morphology of **1** to form electrodeposited **2,** which opens the possibility of increased intermolecular π-π stacking interactions and dimer formation within the metallopolymer matrix, thus resulting in inefficient transport limitations for CO_2 diffusion when compared to 5,5'-ReBpy. This is corroborated by considering the clear difference in the surface film orientation, catalyst packing, and electron density of the respective immobilized complexes (vide supra). Furthermore, it was previously seen for ReBpy species that bipyridine substituents, or anchoring groups, with sufficient electron-withdrawing nature, can induce deleterious effects on CO_2 reduction activity.[73]

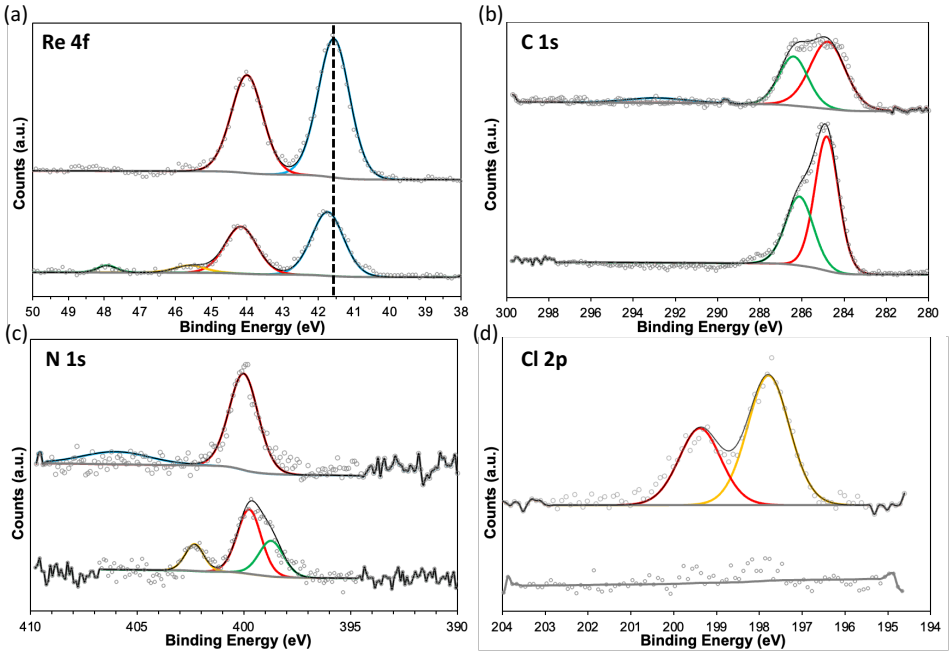

Figure 8. XPS spectra of as prepared electropolymerized **2**-CC-10 (top), **2**-CC-10 after 1 h CPE at -2.6 V in CO_2-saturated 0.1 M $TBAPF_6$ acetonitrile solution (bottom) of (a) High-resolution Re 4f spectra (b) High-resolution C 1s XPS spectra (c) High-resolution N 1s XPS spectra, and (d) High-resolution Cl 2p XPS spectra.

Equally important, post-catalysis characterization was performed with **2**-CC-10 after CPE to probe the stability of **2**. After performing CPE in CO_2-saturated 0.1 M $TBAPF_6$ acetonitrile solution for 1 h, **2**-CC-10 was subjected to C_{dl} measurements, XPS analysis, and the post-catalysis working electrode solution was analyzed with ICP-OES. Post-catalysis C_{dl} measurements revealed little to no loss in ECSA (**Figure 4b**). In addition, ICP-OES analysis of the working electrode solution resulted in no detectable amounts of Re. Moreover, XPS analysis of **2**-CC-10 before and after CPE demonstrated slight structural variations (**Figure 8**). The Re 4f high-resolution spectra display Re 4f peaks that shifted ~0.2 eV higher in BE (**Figure 8a**). The appearance of a peak at 40.6 eV and two peaks at 45.6, and 47.9 eV are attributed to the formation of metallic Re^0 dimer species,[15] and oxide species, respectively.[45] Moreover, examination of the Cl 2p region of post-catalysis **2**-CC-10 suggests that Cl is no longer present after electrolysis (**Figure 8d**). The disappearance of the post-catalysis Cl 2p peak signal signifies a large fraction of **2** participates in the electrolysis, as chloride dissociation is a result of the catalytic single electron reduction.[74] For the Re 4f region, the appearance of a subtle signal at 40.6 eV and signal broadening for the $4f_{7/2}$ peak is due to the formation of surface dimeric Re species. This demonstrates that the surface concentration of dimers increases after electrolysis. Although post-catalysis Re 4f peaks appear diminished in intensity, the peaks still retain sharp symmetry with full-width-half-max (fwhm) values of 1.06 for both Re 4f peaks. The blue-shifted BE values for Re 4f peaks are consistent with the literature values of the exchange of Cl for withdrawing CO generated during CPE.[15] The appearance of Re oxide signals may be a result of the dissociation of Cl, as this would leave active site vacancies, subsequently reacting with oxygen while the sample was exposed to air prior to XPS analysis.

Furthermore, the high-resolution C 1s spectra of **2**-CC-10 displays peaks at 294.7 and 286.8 eV, corresponding to C-C and C-N groups, respectively (**Figure 8b**). After CPE, the peaks associated with the C-C groups become sharper, whereas the peaks associated with the C-N groups decrease in intensity. Additionally, the high-resolution N 1s spectra display a pyridinic nitrogen and $\pi \rightarrow \pi^*$ satellite features at 400.1 and 405.8 eV, respectively. After CPE, there is an appearance of two signals at 402.3 and 398.6 eV. The prior signal is attributed to the intercalation of tetraalkylammonium ions.[15] The latter signal is a result of a change in the pyridinic nitrogen structural environment, also evident from the change in intensity as the N 1s peak at ~400 eV decreases and broadens.

To probe for the cause of deleterious CO_2 reduction activity, the role of substrate depletion was also investigated. As such, a stop-sparge control study was conducted so that two incremental 0.5 h CPE experiments were conducted at -2.6 V, followed by an analysis of the headspace via GC after both CPE runs (**Figure S28** and **Table S7**). The catalytic current was highest in the first 30 min of CPE before a decrease occurred. An increase in the catalytic current was observed upon resparging the H-cell with CO_2 and continuing the electrolysis. Interested in further investigating this, a non-aqueous flow cell was set up to probe the full stability of **2** (***See Supplementary Information***). A constant potential of -2.6 V (referenced to the counter electrode) was applied for a 5 h duration of the electrolysis (**Figure S30**). A current density of ~ –4.5 mA/cm^2 was robustly maintained throughout the electrolysis. Only after 4.5 h does the current density begin to decrease. Moreover, the stability was tested by reusing the same **2**-CC-10 sample for two additional flow-cell experiments (**Figure S30b-c**). The **2**-CC-10 was successfully utilized for two trials without seeing any appreciable decrease in current density (**Figure S30b**). By the third trial, the current density decreased dramatically to ~ –0.7 mA/cm^2, signifying the degradation of the catalyst (**Figure S30c**). This data supports that the initial decrease in CO_2 reduction activity seen for the 1

h CPE experiment was primarily due to substrate depletion and the stability of the catalyst can be maintained over a period of 4 h of electrolysis. This experiment demonstrates a qualitative result of the robust stability of **2**-CC-10. Further optimization of the catalytic parameters (e.g. TON_{CO} and TOF_{CO}) of the CO_2 reduction flow cell is beyond the scope of this paper.

Overall, the post-catalysis investigation demonstrated that **2** experiences stability issues under prolonged electrolysis. There are several possibilities that can contribute to this instability including leaching of the catalyst, catalyst restructuring, or formation of the deleterious Re-Re dimer. Post-catalysis XPS analysis indicates the appearance of a N 1s signal at 398.6 eV, which has been previously attributed to the pyridinic nitrogen component of a demetallated ReBpy complex.[63] However, ICP-OES analysis of the post-catalysis working electrode solution yielded no detectable amounts of Re species. In addition, the retainment of a fwhm = 1.06 for the XPS Re 4f peak suggests that leaching of the catalyst has a negligible contribution to the instability of **2**. As previously discussed, it is apparent that films of **2** form the Re-Re dimeric species. However, the appearance of Re^0 species for the XPS Re 4f region is minute in intensity. Likewise, the recycled use of **2**-CC-10 in a non-aqueous flow cell demonstrates that the CO_2 reduction activity is completely regained after sample exposure to air. This behavior is consistent with electrochemical n-doping.[21] This suggests that the dimer formation minimally contributes to degradation. Therefore, this alludes that the structural change of the surface-bound catalyst likely leads to catalyst deactivation, as seen in previous immobilized systems[21,75] However, the entire perspective for the catalyst deactivation of films of **2** could not be elucidated with the current methods employed here. A more thorough investigation into the other causes of deactivation is required to explain the observations.

CONCLUSIONS:

These studies indicate that the immobilization of molecular catalysts can be successfully optimized for CO_2 reduction. The rhenium [2,2′-bipyridine]-4,4′-diamine complex was successfully converted into the diazonium complex (**1**) and subsequently immobilized via diazonium reductive coupling to generate the grafted film **2**, which was shown to retain the full structural integrity upon electropolymerization. Comparing XPS, UV-Vis, and IRRAS of **2** with that of the analogous 5,5'-ReBpy demonstrates that **2** is less conjugated, more electron deficient at the rhenium center, and the films form aggregations. These results indicate that the electronic communication of the immobilized complex changes as a function of the tethering position of the bipyridine backbone. Also, surface-specific IRRAS studies display substantial changes in the growth morphology for the rhenium [2,2′-bipyridine]-4,4′-bis(diazonium) complex in comparison with the 5,5'-ReBpy analogue. Subsequently, **2** displays a horizontal film growth morphology with respect to the plane of incident (as opposed to parallel growth for 5,5'-ReBpy). Furthermore, electrochemical studies of CV, CPE, EIS, and C_{dl} corroborate the optimal grafting scans as n = 10 scans for both glassy carbon (GC) and carbon cloth (CC) substrates. This corresponds to an optimal loading of 44.6 nmol/cm^2 on CC with TON_{CO} and TOF_{CO} values of 3359 and 0.9 s^{-1}, respectively. The loss of CO_2-reduction efficiency, when compared to the 5,5'-ReBpy analogue, is a result of the formation of aggregation through Re-Re dimer formation and π-π stacking interactions. However, this system demonstrates an active heterogenized CO_2 reduction catalyst cable of robust CO_2 reduction without the need for a Brønsted acid source to promote catalysis.

This work highlights the facile use of molecular immobilization through diazonium coupling to obtain a highly active CO_2 reduction electrocatalyst. In addition, we have demonstrated that a slight change in the tethering position of a heterogenized catalyst can induce drastic changes

in the microenvironment of the catalyst, which can have an immense influence on surface reactivity. This methodology serves as a platform for the surface attachment of molecular catalysts which can be applied to a variety of systems with readily accessible aromatic amines. Thus, this opens the possibility of modulation of the microenvironment through judicious choice of the conductive support, metal center, and ligand structure to further improve CO_2 reduction activity and stability.

ASSOCIATED CONTENT:

Supporting Information:

The following files are available free of charge at (*insert URL of publication*).

^{1}H-NMR, ^{19}F-NMR, ATR-FTIR, IRRAS, UV-Vis, XPS Spectra, SEM, Nyquist plots, **2** surface Re concentrations, additional voltammograms, non-aqueous potentiostatic analysis details, and CPE polarization traces.

AUTHOR INFORMATION:

Corresponding Author

Smaranda C. Marinescu – *Department of Chemistry, University of Southern California, 840 Downey Way, Los Angeles, CA 90089, United States*; ORCID: 0000-0003-2106-8971; ***E-mail: smarines@usc.edu.**

Authors

Jeremiah C. Choate – *Department of Chemistry, University of Southern California, 840 Downey Way, Los Angeles, CA 90089, United States*; ORCID: 0000-0003-2239-2634

Israel Silva Jr. – *Department of Chemistry, University of Southern California, 840 Downey Way, Los Angeles, CA 90089, United States*; ORCID: 0000-0002-6784-0982

Po Ching Hsu – *Loker Hydrocarbon Research Institute, Department of Chemistry, University of Southern California, 837 Bloom Walk, Los Angeles, California 90089, United States*; ORCID: 0009-0006-0216-318X

Kaylyn Tran– *Department of Chemistry, University of Southern California, 840 Downey Way, Los Angeles, CA 90089, United States*; ORCID: 0009-0009-9642-9998

Notes: The authors declare no competing financial interest.

ACKNOWLEDGMENTS:

This work was supported by the University of Southern California (USC) and the National Science Foundation (NSF) through the NSF GRFP award for JCC. The synthesis of the rhenium diamine complexes was supported by the NSF through grant number CHE-2102707. We thank Prof. Jahan

M. Dawlaty for providing access to the IRRAS accessory and to Nicolet™ iS20 FTIR Spectrometer. We also thank Prof. G. K. Surya Prakash and the Loker Hydrocarbon Research Institute at USC for access and assistance with non-aqueous potentiostatic flow-cell system measurements. We thank Cindy Tseng for assistance with IRRAS measurements and for discussion of the results. XPS and SEM data were collected with instrumentation provided by the USC Center of Excellence in Nano Imaging. We thank Tom Czyszczon-Burton for assistance with XPS. UV−vis data were collected with instrumentation provided by USC. NMR data were collected with instrumentation provided by the USC Center of Excellence for Molecular Characterization.

Citations:

(1) van Ruijven, B. J.; De Cian, E.; Sue Wing, I. Amplification of Future Energy Demand Growth Due to Climate Change. *Nat. Commun.* **2019**, *10* (1), 2762. https://doi.org/10.1038/s41467-019-10399-3.

(2) Perez, M.; Perez, R. Update 2022 – A Fundamental Look at Supply Side Energy Reserves for the Planet. *Sol. Energy Adv.* **2022**, *2*, 100014. https://doi.org/10.1016/j.seja.2022.100014.

(3) Borges, C. L. T. An Overview of Reliability Models and Methods for Distribution Systems with Renewable Energy Distributed Generation. *Renew. Sustain. Energy Rev.* **2012**, *16* (6), 4008–4015. https://doi.org/10.1016/j.rser.2012.03.055.

(4) Kumar, B.; Brian, J. P.; Atla, V.; Kumari, S.; Bertram, K. A.; White, R. T.; Spurgeon, J. M. New Trends in the Development of Heterogeneous Catalysts for Electrochemical CO_2 Reduction. *Catal. Today* **2016**, *270*, 19–30. https://doi.org/10.1016/j.cattod.2016.02.006.

(5) Hawecker, J.; Lehn, J.-M.; Ziessel, R. Efficient Photochemical Reduction of CO_2 to CO by Visible Light Irradiation of Systems Containing $Re(Bipy)(CO)_3X$ or $Ru(Bipy)_3^{2+}$–Co^{2+} Combinations as Homogeneous Catalysts. *J. Chem. Soc. Chem. Commun.* **1983**, No. 9, 536–538. https://doi.org/10.1039/C39830000536.

(6) Hawecker, J.; Lehn, J.-M.; Ziessel, R. Electrocatalytic Reduction of Carbon Dioxide Mediated by $Re(Bipy)(CO)_3Cl$ (Bipy = 2,2′-Bipyridine). *J. Chem. Soc. Chem. Commun.* **1984**, No. 6, 328–330. https://doi.org/10.1039/C39840000328.

(7) Sun, L.; Reddu, V.; Fisher, A. C.; Wang, X. Electrocatalytic Reduction of Carbon Dioxide: Opportunities with Heterogeneous Molecular Catalysts. *Energy Environ. Sci.* **2020**, *13* (2), 374–403. https://doi.org/10.1039/C9EE03660A.

(8) Corbin, N.; Zeng, J.; Williams, K.; Manthiram, K. Heterogeneous Molecular Catalysts for Electrocatalytic CO_2 Reduction. *Nano Res.* **2019**, *12* (9), 2093–2125. https://doi.org/10.1007/s12274-019-2403-y.

(9) Eren, E. O.; Özkar, S. Recent Advances in Heterogeneous Catalysts for the Effective Electroreduction of Carbon Dioxide to Carbon Monoxide. *J. Power Sources* **2021**, *506*, 230215. https://doi.org/10.1016/j.jpowsour.2021.230215.

(10) Ye, L.; Liu, J.; Gao, Y.; Gong, C.; Addicoat, M.; Heine, T.; Wöll, C.; Sun, L. Highly Oriented MOF Thin Film-Based Electrocatalytic Device for the Reduction of CO_2 to CO Exhibiting High Faradaic Efficiency. *J. Mater. Chem. A* **2016**, *4* (40), 15320–15326. https://doi.org/10.1039/C6TA04801C.

(11) Johnson, E. M.; Haiges, R.; Marinescu, S. C. Covalent-Organic Frameworks Composed of Rhenium Bipyridine and Metal Porphyrins: Designing Heterobimetallic Frameworks with Two Distinct Metal Sites. *ACS Appl. Mater. Interfaces* **2018**, *10* (44), 37919–37927. https://doi.org/10.1021/acsami.8b07795.

(12) Popov, D. A.; Luna, J. M.; Orchanian, N. M.; Haiges, R.; Downes, C. A.; Marinescu, S. C. A 2,2′-Bipyridine-Containing Covalent Organic Framework Bearing Rhenium(I) Tricarbonyl Moieties for CO_2 Reduction. *Dalton Trans.* **2018**, *47* (48), 17450–17460. https://doi.org/10.1039/C8DT00125A.

(13) Nam, D.-H.; De Luna, P.; Rosas-Hernández, A.; Thevenon, A.; Li, F.; Agapie, T.; Peters, J. C.; Shekhah, O.; Eddaoudi, M.; Sargent, E. H. Molecular Enhancement of Heterogeneous CO_2 Reduction. *Nat. Mater.* **2020**, *19* (3), 266–276. https://doi.org/10.1038/s41563-020-0610-2.

(14) Blakemore, J. D.; Gupta, A.; Warren, J. J.; Brunschwig, B. S.; Gray, H. B. Noncovalent Immobilization of Electrocatalysts on Carbon Electrodes for Fuel Production. *J. Am. Chem. Soc.* **2013**, *135* (49), 18288–18291. https://doi.org/10.1021/ja4099609.
(15) Oh, S.; Gallagher, J. R.; Miller, J. T.; Surendranath, Y. Graphite-Conjugated Rhenium Catalysts for Carbon Dioxide Reduction. *J. Am. Chem. Soc.* **2016**, *138* (6), 1820–1823. https://doi.org/10.1021/jacs.5b13080.
(16) Mahouche-Chergui, S.; Gam-Derouich, S.; Mangeney, C.; Chehimi, M. M. Aryl Diazonium Salts: A New Class of Coupling Agents for Bonding Polymers, Biomacromolecules and Nanoparticles to Surfaces. *Chem. Soc. Rev.* **2011**, *40* (7), 4143–4166. https://doi.org/10.1039/C0CS00179A.
(17) O'Toole, T. R.; Sullivan, B. P.; Bruce, M. R.-M.; Margerum, L. D.; Murray, R. W.; Meyer, T. J. Electrocatalytic Reduction of CO_2 by a Complex of Rhenium in Thin Polymeric Films. *J. Electroanal. Chem. Interfacial Electrochem.* **1989**, *259* (1), 217–239. https://doi.org/10.1016/0022-0728(89)80049-X.
(18) Delamar, M.; Hitmi, R.; Pinson, J.; Saveant, J. M. Covalent Modification of Carbon Surfaces by Grafting of Functionalized Aryl Radicals Produced from Electrochemical Reduction of Diazonium Salts. *J. Am. Chem. Soc.* **1992**, *114* (14), 5883–5884. https://doi.org/10.1021/ja00040a074.
(19) Sun, C.; Rotundo, L.; Garino, C.; Nencini, L.; Yoon, S. S.; Gobetto, R.; Nervi, C. Electrochemical CO_2 Reduction at Glassy Carbon Electrodes Functionalized by MnI and ReI Organometallic Complexes. *ChemPhysChem* **2017**, *18* (22), 3219–3229. https://doi.org/10.1002/cphc.201700739.
(20) Chan, W. K. Metal Containing Polymers with Heterocyclic Rigid Main Chains. *Coord. Chem. Rev.* **2007**, *251* (17), 2104–2118. https://doi.org/10.1016/j.ccr.2007.03.002.
(21) Orchanian, N. M.; Hong, L. E.; Skrainka, J. A.; Esterhuizen, J. A.; Popov, D. A.; Marinescu, S. C. Surface-Immobilized Conjugated Polymers Incorporating Rhenium Bipyridine Motifs for Electrocatalytic and Photocatalytic CO_2 Reduction. *ACS Appl. Energy Mater.* **2019**, *2* (1), 110–123. https://doi.org/10.1021/acsaem.8b01745.
(22) Hellman, A. N.; Intrator, J. A.; Choate, J. C.; Velazquez, D. A.; Marinescu, S. C. Primary- and Secondary-Sphere Effects of Amine Substituent Position on Rhenium Bipyridine Electrocatalysts for CO_2 Reduction. *Polyhedron* **2022**, *223*, 115933. https://doi.org/10.1016/j.poly.2022.115933.
(23) Marshall, N.; Locklin, J. Reductive Electrografting of Benzene (p-Bisdiazonium Hexafluorophosphate): A Simple and Effective Protocol for Creating Diazonium-Functionalized Thin Films. *Langmuir* **2011**, *27* (21), 13367–13373. https://doi.org/10.1021/la2024617.
(24) Hayashi, Y.; Kita, S.; Brunschwig, B. S.; Fujita, E. Involvement of a Binuclear Species with the Re−C(O)O−Re Moiety in CO2 Reduction Catalyzed by Tricarbonyl Rhenium(I) Complexes with Diimine Ligands: Strikingly Slow Formation of the Re−Re and Re−C(O)O−Re Species from Re(Dmb)$(CO)_3$S (Dmb = 4,4'-Dimethyl-2,2'-Bipyridine, S = Solvent). *J. Am. Chem. Soc.* **2003**, *125* (39), 11976–11987. https://doi.org/10.1021/ja035960a.
(25) Manbeck, G. F.; Muckerman, J. T.; Szalda, D. J.; Himeda, Y.; Fujita, E. Push or Pull? Proton Responsive Ligand Effects in Rhenium Tricarbonyl CO_2 Reduction Catalysts. *J. Phys. Chem. B* **2015**, *119* (24), 7457–7466. https://doi.org/10.1021/jp511131x.

(26) Pinson, J.; Podvorica, F. Attachment of Organic Layers to Conductive or Semiconductive Surfaces by Reduction of Diazonium Salts. *Chem. Soc. Rev.* **2005**, *34* (5), 429–439. https://doi.org/10.1039/B406228K.
(27) Vlček, A. Ultrafast Excited-State Processes in Re(I) Carbonyl-Diimine Complexes: From Excitation to Photochemistry. In *Photophysics of Organometallics*; Lees, A. J., Ed.; Springer: Berlin, Heidelberg, 2010; pp 115–158. https://doi.org/10.1007/3418_2009_4.
(28) Yang, L.; Ren, A.-M.; Feng, J.-K.; Liu, X.-J.; Ma, Y.-G.; Zhang, M.; Liu, X.-D.; Shen, J.-C.; Zhang, H.-X. Theoretical Studies of Ground and Excited Electronic States in a Series of Halide Rhenium(I) Bipyridine Complexes. *J. Phys. Chem. A* **2004**, *108* (32), 6797–6808. https://doi.org/10.1021/jp0357727.
(29) Tignor, S. E.; Kuo, H.-Y.; Lee, T. S.; Scholes, G. D.; Bocarsly, A. B. Manganese-Based Catalysts with Varying Ligand Substituents for the Electrochemical Reduction of CO_2 to CO. *Organometallics* **2019**, *38* (6), 1292–1299. https://doi.org/10.1021/acs.organomet.8b00554.
(30) Lees, A. J. *Photophysics of Organometallics*; Springer Science & Business Media, 2010.
(31) Su, W.-F. Characterization of Polymer. In *Principles of Polymer Design and Synthesis*; Su, W.-F., Ed.; Lecture Notes in Chemistry; Springer: Berlin, Heidelberg, 2013; pp 89–110. https://doi.org/10.1007/978-3-642-38730-2_5.
(32) Kurtz, D. A.; Brereton, K. R.; Ruoff, K. P.; Tang, H. M.; Felton, G. A. N.; Miller, A. J. M.; Dempsey, J. L. Bathochromic Shifts in Rhenium Carbonyl Dyes Induced through Destabilization of Occupied Orbitals. *Inorg. Chem.* **2018**, *57* (9), 5389–5399. https://doi.org/10.1021/acs.inorgchem.8b00360.
(33) Fernández-Terán, R. J.; Sucre-Rosales, E.; Echevarria, L.; Hernández, F. E. Dissecting Conjugation and Electronic Effects on the Linear and Non-Linear Optical Properties of Rhenium(I) Carbonyl Complexes. *Phys. Chem. Chem. Phys.* **2022**, *24* (45), 28069–28079. https://doi.org/10.1039/D2CP03844G.
(34) Allongue, P.; Delamar, M.; Desbat, B.; Fagebaume, O.; Hitmi, R.; Pinson, J.; Savéant, J.-M. Covalent Modification of Carbon Surfaces by Aryl Radicals Generated from the Electrochemical Reduction of Diazonium Salts. *J. Am. Chem. Soc.* **1997**, *119* (1), 201–207. https://doi.org/10.1021/ja963354s.
(35) Ceccato, M.; Bousquet, A.; Hinge, M.; Pedersen, S. U.; Daasbjerg, K. Using a Mediating Effect in the Electroreduction of Aryldiazonium Salts To Prepare Conducting Organic Films of High Thickness. *Chem. Mater.* **2011**, *23* (6), 1551–1557. https://doi.org/10.1021/cm1033244.
(36) Tiddia, M.; Mula, G.; Mascia, M.; Sechi, E.; Vacca, A. Porous Silicon–Polyaniline Hybrid Composites Synthesized through Electroreduction of an Aryldiazonium Salt: Preparation and Photocurrent Properties. *RSC Adv.* **2016**, *6* (104), 101880–101887. https://doi.org/10.1039/C6RA19868F.
(37) Swallow, J. E. N.; Williamson, B. A. D.; Whittles, T. J.; Birkett, M.; Featherstone, T. J.; Peng, N.; Abbott, A.; Farnworth, M.; Cheetham, K. J.; Warren, P.; Scanlon, D. O.; Dhanak, V. R.; Veal, T. D. Self-Compensation in Transparent Conducting F-Doped SnO_2. *Adv. Funct. Mater.* **2018**, *28* (4), 1701900. https://doi.org/10.1002/adfm.201701900.
(38) Collins, G.; Fleming, P.; O'Dwyer, C.; Morris, M. A.; Holmes, J. D. Organic Functionalization of Germanium Nanowires Using Arenediazonium Salts. *Chem. Mater.* **2011**, *23* (7), 1883–1891. https://doi.org/10.1021/cm103573m.

(39) Jousselme, B.; Bidan, G.; Billon, M.; Goyer, C.; Kervella, Y.; Guillerez, S.; Hamad, E. A.; Goze-Bac, C.; Mevellec, J.-Y.; Lefrant, S. One-Step Electrochemical Modification of Carbon Nanotubes by Ruthenium Complexes via New Diazonium Salts. *J. Electroanal. Chem.* **2008**, *621* (2), 277–285. https://doi.org/10.1016/j.jelechem.2008.01.026.
(40) Denisevich, P.; Abruna, H. D.; Leidner, C. R.; Meyer, T. J.; Murray, R. W. Electropolymerization of Vinylpyridine and Vinylbipyridine Complexes of Iron and Ruthenium: Homopolymers, Copolymers, Reactive Polymers. *Inorg. Chem.* **1982**, *21* (6), 2153–2161. https://doi.org/10.1021/ic00136a006.
(41) Mesnage, A.; Lefèvre, X.; Jégou, P.; Deniau, G.; Palacin, S. Spontaneous Grafting of Diazonium Salts: Chemical Mechanism on Metallic Surfaces. *Langmuir* **2012**, *28* (32), 11767–11778. https://doi.org/10.1021/la3011103.
(42) Gardella, J. A.; Ferguson, S. A.; Chin, R. L. π*← π Shakeup Satellites for the Analysis of Structure and Bonding in Aromatic Polymers by X-Ray Photoelectron Spectroscopy. *Appl. Spectrosc.* **1986**, *40* (2), 224–232. https://doi.org/10.1366/0003702864509565.
(43) *Handbook of X-Ray Photoelectron Spectroscopy: A Reference Book of Standard Spectra for Identification and Interpretation of XPS Data*, Update.; Moulder, J. F., Chastain, J., Eds.; Perkin-Elmer Corporation: Eden Prairie, Minn, 1992.
(44) Permatasari, F. A.; Aimon, A. H.; Iskandar, F.; Ogi, T.; Okuyama, K. Role of C–N Configurations in the Photoluminescence of Graphene Quantum Dots Synthesized by a Hydrothermal Route. *Sci. Rep.* **2016**, *6* (1), 21042. https://doi.org/10.1038/srep21042.
(45) Greiner, M. T.; Rocha, T. C. R.; Johnson, B.; Klyushin, A.; Knop-Gericke, A.; Schlögl, R. The Oxidation of Rhenium and Identification of Rhenium Oxides During Catalytic Partial Oxidation of Ethylene: An In-Situ XPS Study. *Z. Für Phys. Chem.* **2014**, *228* (4–5), 521–541. https://doi.org/10.1515/zpch-2014-0002.
(46) Ng, P. K.; Gong, X.; Chan, S. H.; Lam, L. S. M.; Chan, W. K. The Role of Ruthenium and Rhenium Diimine Complexes in Conjugated Polymers That Exhibit Interesting Opto-Electronic Properties. *Chem. – Eur. J.* **2001**, *7* (20), 4358–4367. https://doi.org/10.1002/1521-3765(20011015)7:20<4358::AID-CHEM4358>3.0.CO;2-M.
(47) Kirgan, R. A.; Sullivan, B. P.; Rillema, D. P. Photochemistry and Photophysics of Coordination Compounds: Rhenium. In *Photochemistry and Photophysics of Coordination Compounds II*; Balzani, V., Campagna, S., Eds.; Topics in Current Chemistry; Springer: Berlin, Heidelberg, 2007; pp 45–100. https://doi.org/10.1007/128_2007_143.
(48) Ley, K. D.; Whittle, C. E.; Bartberger, M. D.; Schanze, K. S. Photophysics of π-Conjugated Polymers That Incorporate Metal to Ligand Charge Transfer Chromophores. *J. Am. Chem. Soc.* **1997**, *119* (14), 3423–3424. https://doi.org/10.1021/ja963278t.
(49) Liard, D. J.; Vlček, A. Picosecond Dynamics of Photoinduced Interligand Electron Transfer in $[Re(MQ^+)(CO)_3(Dmb)]^{2+}$ (Dmb = 4,4‘-Dimethyl-2,2‘-Bipyridine, MQ^+ = N-Methyl-4,4‘-Bipyridinium). *Inorg. Chem.* **2000**, *39* (3), 485–490. https://doi.org/10.1021/ic990770f.
(50) Gabrielsson, A.; Busby, M.; Matousek, P.; Towrie, M.; Hevia, E.; Cuesta, L.; Perez, J.; Záliš, S.; Vlček, A. Electronic Structure and Excited States of Rhenium(I) Amido and Phosphido Carbonyl−Bipyridine Complexes Studied by Picosecond Time-Resolved IR Spectroscopy and DFT Calculations. *Inorg. Chem.* **2006**, *45* (24), 9789–9797. https://doi.org/10.1021/ic0614768.
(51) Fujita, E.; Muckerman, J. T. Why Is Re−Re Bond Formation/Cleavage in $[Re(Bpy)(CO)_3]_2$ Different from That in $[Re(CO)_5]_2$? Experimental and Theoretical Studies

on the Dimers and Fragments. *Inorg. Chem.* **2004**, *43* (24), 7636–7647. https://doi.org/10.1021/ic048910v.
(52) O'Toole, T. R.; Sullivan, B. P.; Meyer, T. J. Organometallic Photochemistry in Thin Polymeric Films. Photoimaging. *J. Am. Chem. Soc.* **1989**, *111* (15), 5699–5706. https://doi.org/10.1021/ja00197a030.
(53) Yin, H.; Yang, T.; Wang, K.-Z.; Tong, J.; Yu, S.-Y. Unusual Photoelectrochemical Properties of Electropolymerized Films of a Triphenylamine-Containing Organic Small Molecule. *Langmuir* **2019**, *35* (39), 12620–12629. https://doi.org/10.1021/acs.langmuir.9b01578.
(54) Kalyanasundaram, K.; Nazeeruddin, Md. K. Tuning of the CT Excited State and Validity of the Energy Gap Law in Mixed Ligand Complexes of Ru(II) Containing 4,4′-Dicarboxy-2,2′-Bipyridine. *Chem. Phys. Lett.* **1992**, *193* (4), 292–297. https://doi.org/10.1016/0009-2614(92)85670-6.
(55) Ricks, A. M.; Anfuso, C. L.; Rodríguez-Córdoba, W.; Lian, T. Vibrational Relaxation Dynamics of Catalysts on TiO_2 Rutile (110) Single Crystal Surfaces and Anatase Nanoporous Thin Films. *Chem. Phys.* **2013**, *422*, 264–271. https://doi.org/10.1016/j.chemphys.2013.04.001.
(56) Kiefer, L. M.; King, J. T.; Kubarych, K. J. Dynamics of Rhenium Photocatalysts Revealed through Ultrafast Multidimensional Spectroscopy. *Acc. Chem. Res.* **2015**, *48* (4), 1123–1130. https://doi.org/10.1021/ar500402r.
(57) Laaser, J. E.; Christianson, J. R.; Oudenhoven, T. A.; Joo, Y.; Gopalan, P.; Schmidt, J. R.; Zanni, M. T. Dye Self-Association Identified by Intermolecular Couplings between Vibrational Modes As Revealed by Infrared Spectroscopy, and Implications for Electron Injection. *J. Phys. Chem. C* **2014**, *118* (11), 5854–5861. https://doi.org/10.1021/jp412402v.
(58) Oudenhoven, T. A.; Joo, Y.; Laaser, J. E.; Gopalan, P.; Zanni, M. T. Dye Aggregation Identified by Vibrational Coupling Using 2D IR Spectroscopy. *J. Chem. Phys.* **2015**, *142* (21), 212449. https://doi.org/10.1063/1.4921649.
(59) Kraack, J. P.; Hamm, P. Solvent-Controlled Morphology of Catalytic Monolayers at Solid–Liquid Interfaces. *J. Phys. Chem. C* **2018**, *122* (4), 2259–2267. https://doi.org/10.1021/acs.jpcc.7b12421.
(60) Flach, C. R.; Gericke, A.; Mendelsohn, R. Quantitative Determination of Molecular Chain Tilt Angles in Monolayer Films at the Air/Water Interface: Infrared Reflection/Absorption Spectroscopy of Behenic Acid Methyl Ester. *J. Phys. Chem. B* **1997**, *101* (1), 58–65. https://doi.org/10.1021/jp962288d.
(61) Mendelsohn, R.; Mao, G.; Flach, C. R. Infrared Reflection–Absorption Spectroscopy: Principles and Applications to Lipid–Protein Interaction in Langmuir Films. *Biochim. Biophys. Acta BBA - Biomembr.* **2010**, *1798* (4), 788–800. https://doi.org/10.1016/j.bbamem.2009.11.024.
(62) Benson, E. E.; Kubiak, C. P. Structural Investigations into the Deactivation Pathway of the CO_2 Reduction Electrocatalyst $Re(Bpy)(CO)_3Cl$. *Chem. Commun.* **2012**, *48* (59), 7374–7376. https://doi.org/10.1039/C2CC32617E.
(63) Bartl, J. D.; Thomas, C.; Henning, A.; Ober, M. F.; Savasci, G.; Yazdanshenas, B.; Deimel, P. S.; Magnano, E.; Bondino, F.; Zeller, P.; Gregoratti, L.; Amati, M.; Paulus, C.; Allegretti, F.; Cattani-Scholz, A.; Barth, J. V.; Ochsenfeld, C.; Nickel, B.; Sharp, I. D.; Stutzmann, M.; Rieger, B. Modular Assembly of Vibrationally and Electronically Coupled

Rhenium Bipyridine Carbonyl Complexes on Silicon. *J. Am. Chem. Soc.* **2021**, *143* (46), 19505–19516. https://doi.org/10.1021/jacs.1c09061.
(64) Gamini Rajapakse, R. M.; L. Watkins, D.; A. Ranathunge, T.; U. Malikaramage, A.; P. Gunarathna, H. M. N.; Sandakelum, L.; Wylie, S.; R. Abewardana, P. G. P.; K. Egodawele, M. G. S. a. M. E. W. D. D.; K. Herath, W. H. M. R. N.; V. Bandara, S.; R. Strongin, D.; Harsha Attanayake, N.; Velauthapillai, D.; R. Horrocks, B. Implementing the Donor–Acceptor Approach in Electronically Conducting Copolymers via Electropolymerization. *RSC Adv.* **2022**, *12* (19), 12089–12115. https://doi.org/10.1039/D2RA01176J.
(65) Yamamoto, T.; Maruyama, T.; Zhou, Z.-H.; Ito, T.; Fukuda, T.; Yoneda, Y.; Begum, F.; Ikeda, T.; Sasaki, S. π-Conjugated Poly(pyridine-2,5-diyl), Poly(2,2'-bipyridine-5,5'-diyl), and Their Alkyl Derivatives. Preparation, Linear Structure, Function as a Ligand to Form Their Transition Metal Complexes, Catalytic Reactions, n-Type Electrically Conducting Properties, Optical Properties, and Alignment on Substrates. *J. Am. Chem. Soc.* **1994**, *116* (11), 4832–4845. https://doi.org/10.1021/ja00090a031.
(66) McCrory, C. C. L.; Jung, S.; Peters, J. C.; Jaramillo, T. F. Benchmarking Heterogeneous Electrocatalysts for the Oxygen Evolution Reaction. *J. Am. Chem. Soc.* **2013**, *135* (45), 16977–16987. https://doi.org/10.1021/ja407115p.
(67) Orchanian, N. M.; Hong, L. E.; Marinescu, S. C. Immobilized Molecular Wires on Carbon-Cloth Electrodes Facilitate CO_2 Electrolysis. *ACS Catal.* **2019**, *9* (10), 9393–9397. https://doi.org/10.1021/acscatal.9b03134.
(68) Rotundo, L.; Filippi, J.; Gobetto, R.; Miller, H. A.; Rocca, R.; Nervi, C.; Vizza, F. Electrochemical CO_2 Reduction in Water at Carbon Cloth Electrodes Functionalized with a Fac-Mn(Apbpy)$(CO)_3$Br Complex. *Chem. Commun.* **2019**, *55* (6), 775–777. https://doi.org/10.1039/C8CC08385A.
(69) Willkomm, J.; Bouzidi, S.; Bertin, E.; Birss, V. I.; Piers, W. E. Aqueous CO_2 Reduction by a Re(Bipyridine)-Polypyrrole Film Deposited on Colloid-Imprinted Carbon. *ACS Catal.* **2021**, *11* (3), 1096–1105. https://doi.org/10.1021/acscatal.0c04035.
(70) Liu, S.; Lu, X. F.; Xiao, J.; Wang, X.; Lou, X. W. (David). Bi_2O_3 Nanosheets Grown on Multi-Channel Carbon Matrix to Catalyze Efficient CO_2 Electroreduction to HCOOH. *Angew. Chem. Int. Ed.* **2019**, *58* (39), 13828–13833. https://doi.org/10.1002/anie.201907674.
(71) Zhao, Y.; Pei, Z.; Lu, X. F.; Luan, D.; Wang, X.; Lou, X. W. (David). Rationally Designed Nitrogen-Doped Carbon Macroporous Fibers with Loading of Single Cobalt Sites for Efficient Aqueous Zn-CO_2 Batteries. *Chem Catal.* **2022**, *2* (6), 1480–1493. https://doi.org/10.1016/j.checat.2022.05.015.
(72) Zhu, M.; Chen, J.; Huang, L.; Ye, R.; Xu, J.; Han, Y.-F. Covalently Grafting Cobalt Porphyrin onto Carbon Nanotubes for Efficient CO_2 Electroreduction. *Angew. Chem. Int. Ed.* **2019**, *58* (20), 6595–6599. https://doi.org/10.1002/anie.201900499.
(73) Guyot, M.; Lalloz, M.-N.; Aguirre-Araque, J. S.; Rogez, G.; Costentin, C.; Chardon-Noblat, S. Rhenium Carbonyl Molecular Catalysts for CO_2 Electroreduction: Effects on Catalysis of Bipyridine Substituents Mimicking Anchorage Functions to Modify Electrodes. *Inorg. Chem.* **2022**, *61* (40), 16072–16080. https://doi.org/10.1021/acs.inorgchem.2c02473.
(74) Zhanaidarova, A.; Jones, S. C.; Despagnet-Ayoub, E.; Pimentel, B. R.; Kubiak, C. P. Re(*t*Bu-Bpy)$(CO)_3$Cl Supported on Multi-Walled Carbon Nanotubes Selectively Reduces CO_2 in Water. *J. Am. Chem. Soc.* **2019**, *141* (43), 17270–17277. https://doi.org/10.1021/jacs.9b08445.

(75) Schreier, M.; Luo, J.; Gao, P.; Moehl, T.; Mayer, M. T.; Grätzel, M. Covalent Immobilization of a Molecular Catalyst on Cu_2O Photocathodes for CO_2 Reduction. *J. Am. Chem. Soc.* **2016**, *138* (6), 1938–1946. https://doi.org/10.1021/jacs.5b12157.

Table of Contents (TOC) Abstract Graphics